Manuscript Details

Manuscript number IJEPES_2019_1505

Title Induction Machine Model with Space Harmonics for the Diagnosis of Rotor Eccentricity, based on the Convolution Theorem

Article type Research paper

Abstract

Condition based maintenance systems (CBM) of induction machines (IMs) require fast and accurate models that can reproduce the fault related harmonics generated by different kinds of faults, in order to help in developing new diagnostic algorithms for detecting the faults at an early stage, to analyse the physical interactions between simultaneous faults of different types, or to train expert systems that can supervise and identify these faults in an autonomous way. To achieve these goals, such models must take into account the space harmonics of the air gap magnetomotive force (MMF) generated by the machine windings under fault conditions, due to the complex interactions between spatial and time harmonics in a faulty machine. One of the most common faults in induction machines is the rotor eccentricity, which can cause significant radial forces and, in extreme cases, produce destructive rotor-stator rub. But the development of a fast, analytic model of the eccentric IM is a challenging task, due to the non-uniformity of the air gap. In this paper, a new method is proposed to obtain such a fast model. This method, which is theoretically justified, enables a fast calculation of the self and mutual inductances of the stator and rotor phases for every rotor position. The proposed method is validated first using a finite elements method (FEM) model, and then, through an experimental test-bed using commercial induction motors with a forced mixed eccentricity fault.

Keywords induction machines; convolution; discrete Fourier transforms; fault diagnosis; air gap eccentricity.

Corresponding Author Manuel Pineda-Sánchez

Corresponding Author's Institution upv

Order of Authors Angel Sapena-Bañó, Javier Martinez-Roman, Ruben Puche-Panadero, Manuel Pineda-Sánchez, Juan Perez-Cruz, martin riera-guasp

Suggested reviewers Emilio Gomez-Lazaro

Submission Files Included in this PDF

File Name [File Type]

cover_letter.pdf [Cover Letter]

highlights.docx [Highlights]

Induction Machine Model for the Diagnosis of Rotor Eccentricity.pdf [Manuscript File]

Submission Files Not Included in this PDF

File Name [File Type]

Induction Machine Model for the Diagnosis of Rotor Eccentricity.zip [LaTeX Source File]

To view all the submission files, including those not included in the PDF, click on the manuscript title on your EVISE Homepage, then click 'Download zip file'.

Cover Letter

Dear Editor,

We are pleased to submit the manuscript entitled “Induction Machine Model with Space Harmonics for the Diagnosis of Rotor Eccentricity, based on the Convolution Theorem”, to be considered for publication in International Journal of Electrical Power & Energy Systems.

I, as corresponding author on behalf of all the authors, hereby provide information regarding that this manuscript has been only submitted to this journal and there is not another submitted version to other journals.

Sincerely,

Manuel Pineda-Sanchez

Corresponding Author:

Manuel Pineda-Sanchez
Institute for Energy Engineering
Universitat Politècnica de València
Camino de Vera s/n
46022 Valencia, Spain
Phone 34 96 387 96 40
Fax 34 96 387 75 99
Email: mpineda@die.upv.es

Authors (in signature order):

Angel Sapena-Bano
Institute for Energy Engineering
Universitat Politècnica de València
Valencia, Spain
Email: asapena@die.upv.es

Javier Martinez-Roman
Institute for Energy Engineering
Universitat Politècnica de València
Valencia, Spain
Email: jmroman@die.upv.es

Ruben Puche-Panadero, Member of IEEE
Institute for Energy Engineering
Universitat Politècnica de València

Valencia, Spain
Email: rupucpa@die.upv.es

Manuel Pineda-Sanchez
Institute for Energy Engineering
Universitat Politècnica de València
Valencia, Spain
Email: mpineda@die.upv.es

Juan Perez-Cruz
Institute for Energy Engineering
Universitat Politècnica de València
Valencia, Spain
Email: juperez@die.upv.es

Martin Riera-Guasp
Institute for Energy Engineering
Universitat Politècnica de València
Valencia, Spain
Email: mriera@die.upv.es

- The yoke flux of a conductor in an eccentric machine is obtained analytically.
- A single formula gives the inductance between two phases for every rotor position,
- This formula is the convolution of the conductors' distributions and the yoke flux.
- The convolution is computed as a pointwise multiplication in the frequency domain.
- The fast Fourier transform is used to switch between spatial and frequency domains.

Induction Machine Model with Space Harmonics for the Diagnosis of Rotor Eccentricity, based on the Convolution Theorem

A. Sapena-Bano, J. Martinez-Roman, R. Puche-Panadero, M. Pineda-Sanchez*, J. Perez-Cruz, M. Riera-Guasp

Institute for Energy Engineering, Universitat Politècnica de València, Cmno. de Vera s/n, 46022 Valencia, Spain

---

Abstract

Condition based maintenance systems (CBM) of induction machines (IMs) require fast and accurate models that can reproduce the fault related harmonics generated by different kinds of faults, in order to help in developing new diagnostic algorithms for detecting the faults at an early stage, to analyse the physical interactions between simultaneous faults of different types, or to train expert systems that can supervise and identify these faults in an autonomous way. To achieve these goals, such models must take into account the space harmonics of the air gap magnetomotive force (MMF) generated by the machine windings under fault conditions, due to the complex interactions between spatial and time harmonics in a faulty machine. One of the most common faults in induction machines is the rotor eccentricity, which can cause significant radial forces and, in extreme cases, produce destructive rotor-stator rub. But the development of a fast, analytic model of the eccentric IM is a challenging task, due to the non-uniformity of the air gap. In this paper, a new method is proposed to obtain such a fast model. This method, which is theoretically justified, enables a fast calculation of the self and mutual inductances of the stator and rotor phases for every rotor posi-

*Corresponding author

Email addresses: asapena@die.upv.es (A. Sapena-Bano), jmroman@die.upv.es (J. Martinez-Roman), rupucpa@die.upv.es (R. Puche-Panadero), mpineda@die.upv.es (M. Pineda-Sanchez), juperez@die.upv.es (J. Perez-Cruz), mriera@die.upv.es (M. Riera-Guasp)

Preprint submitted to INTERNATIONAL JOURNAL OF ELECTRICAL POWER & ENERGY SYSTEMS May 6, 20

tion. The proposed method is validated first using a finite elements method (FEM) model, and then, through an experimental test-bed using commercial induction motors with a forced mixed eccentricity fault.

Keywords: Inductance, Induction Machines, Convolution, Discrete Fourier Transforms, Fault Diagnosis, Air Gap Eccentricity

---

1. Introduction

Induction machines (IMs) are present in most industrial processes, either as driving motors [1, 2] or as generating units [3–5]. Their preponderance relies on their inherent robustness and reliability. Nevertheless, they are subjected to mechanical and electrical ageing, with the risk of suffering different kinds of faults during their operational life. Their unexpected failure can provoke heavy economical losses, depending on its impact on the sudden stoppage of the production lines or the power generating stations. The implementation of CBM systems for IMs [6] can reduce these risks, with the goal of detecting machine problems prior to failure [7], and can also help to optimize the schedule of maintenance stops, with the goal of reducing the production losses during the stop. From a broader point of view, CBM systems for IMs can be integrated in maintenance systems for electrical installations, along with CBMs for inverters [8], generators [9], transformers [10–13], power systems [14], transmission lines [15, 16] or microgrids [17, 18].

Different techniques that can be used for implementing a CBM system for IMs [19], such as the analysis of currents [20–24], vibrations [24–27], instantaneous power [28], reactive power [29], apparent power [21], voltages [30, 31], back EMFs induced tooth-coil windings [32, 33], voltage injection [34], thermal images [35, 36], internal flux [37, 38], acoustic emissions [39, 40], etc. Among these methods, the analysis of the machine current signature (MCSA) method has attracted an special interest [24, 41], because it is non invasive (it requires only a current probe that can be attached to the line which feeds the machine), fast an easy to implement online (it uses a FFT to obtain the current spectrum, where the characteristic fault signatures can be detected), and is able to detect different, and possibly simultaneous [42–44], types of faults, and it can be operated on line. In spite of its conceptual simplicity, the practical application of MCSA in harsh industrial environments is a challenging issue. The amplitude of the fault harmonics is very small, compared with the fundamental component, so that electromagnetic noise produced by electronic converters [45, 46], harmonics generated by oscillating loads, or even the spectral leakage of the FFT can hide the fault harmonics generated by the fault, avoiding its detection until the fault is severe. The use of a fast, analytical model that can reproduce the fault harmonics in the current spectra, under many different controlled working conditions, becomes then a valuable resource for the development of robust MCSA algorithms and expert systems for CBM systems [5, 47–49].

Eccentricity is a common type of IM fault [21, 28, 29, 50–55], which is caused primarily because of maladjustment of bearings, load imbalance, shaft flexibility, thermal deformations, or misalignments [56]. The asymmetry of the magnetic field in the non-uniform air gap of the eccentric IM produces radial forces [53], that is, an unbalanced magnetic pull (UMP) [57–61], which generates abnormal vibrations, damages in the shaft bearings, destructive rotor-stator rub [62] or even sparks during the starting of the motor [63].

Diverse models of the eccentric IM have been proposed recently. The most accurate ones are based in the finite elements method (FEM). Transient finite-element models of the eccentric IM have been applied to assess the influence on the UMP of the series/parallel winding connections [64]. A time-stepping FEM model is used in [65] to analyze the influence of load variation on the diagnostic indexes of an eccentric motor; in [53] to compute the power balance of an eccentric IM; and in [66] to obtain the characteristic harmonic components generated by an eccentricity fault. Despite its great accuracy, FEM models of an eccentric IM require important computer resources and computing time. To overcome this drawback, an hybrid FEM/superposition approach is proposed in [67], which is able to model an eccentric motor with a saving in time of several orders of magnitude, with a mere 3% of relative error compared with a full FEM model. In [33] a 3D field reconstruction method (3D-FRM)is applied to built stator and rotor basis using reduced number of FEM simulations, which provides the same accuracy as 3-D FEM at a lower computational cost. To further reduce the computing requirements, in time and memory resources of the FEM model of the eccentric IM, several analytic models have been presented in the technical literature, with times of calculation several orders of magnitude lower than in the case of FEM models, while maintaining a similar level of accuracy regarding the calculation of fault harmonics. For example, [68] reports a few seconds for the analytical model versus more than three hours for the FEM model, and [69] reports 4 minutes for the analytical model versus 50 hours for the equivalent FEM model. A 3D magnetic equivalent circuit model has been presented in [70], as a high resolution analytical replacement of FEM models. Nevertheless, in most cases simpler 2D equivalent circuit models are used for diagnostic purposes. One approach for building such 2D analytical models relies on finding the analytical solution of the magnetic field in the air-gap of the eccentric machine [71]. In [37] this solution is obtained considering only the fundamental component of the stator airgap flux density, and in in [72–76] a conformal transformation is applied to the expressions of the magnetic field of a healthy machine. Nevertheless, the conformal transformations presented in these works result in infinite series expansions for the air-gap magnetic field, which converge slowly. Other approaches make use of the inverse air-gap function of the eccentric machine to compute the matrix of phase inductances, via a modified winding function approach (MWFA), as in [4, 20, 51, 54, 77–80]. But MWFA has some drawbacks: to account for coil pitch, slot skewing or the rise of the air gap MMF across the slot, different winding functions must be used in each case. Besides, the winding function of a phase must be computed using both the winding functions of the coils that constitute the phase and the coils distribution. Finally, the winding functions must be integrated to obtain the phases inductances, and complex integrals must be solved in this process, which may be very cumbersome in the case of arbitrary winding distributions. As it is stated in [81], this task typically consumes a high amount of time, so that only discrete curves of inductance versus rotor position are calculated and linear interpolation is applied at intermediate rotor positions. But this approach requires different winding functions for each type of winding, and difficult its application for complex winding distributions.

In a previous paper [82], after a critical review of the MWFA, a completely different way of attacking the problem was under-taken and a new method for computing winding inductances in uniform air gap machines was presented and developed. In this paper, the method introduced in [82] is extended to include the effects of static and dynamic eccentricity, in a two stage process:

- First, a novel analytical expression is derived for representing the yoke flux generated by a single conductor, placed at any angular position in the air-gap, for any rotor position and for any degree of eccentricity.

- And, second, a new procedure, based on the spatial convolution of this expression and the distributions of the phases conductors, is developed for obtaining the phases inductances of the eccentric IM, which are used in the equivalent circuit model. This new procedure is expressed as a single equation which gives the mutual inductances of two phases corresponding to all of their possible relative positions, and for all of the rotor positions, taking into account the air gap MMF harmonics. This algorithm it is very fast, because it is based on the FFT. And the calculation time is independent of the complexity of the windings layout.

The structure of this paper is as follows: in Section 2 the general system equations for an induction machine are briefly reminded, since they are the base of subsequent developments and also for introducing the nomenclature. In Section 3, the inverse air-gap function of the eccentric IM is presented, and in Section 4 it is used for deriving the general expression of the yoke flux generated by a single conductor in an eccentric IM, for any position of the rotor centre, and for any degree of eccentricity. Section 5 establishes the relationship between the rotor centre coordinates and the rotor turning position, depending on the type of eccentricity, static, dynamic or mixed. Both expressions are combined in Section 6, using a new convolution-based method, for obtaining the mutual inductance between every two phases of the machine for any relative angular position, and for any rotor position, and in Section 7, it is implemented using the FFT. The proposed method is validated in Section 8, comparing it with numerical results obtained through a FEM model, and through experimental results obtained with a commercial IM with a forced eccentricity fault. Finally, in Section 9, the conclusions of this work are presented.

2. Induction Machines General Electromechanical Equations System

The following equations system [83–85] can be written for an induction machine with m stator and n rotor phases with arbitrary layout (that is, even under winding fault conditions like inter-turn short circuits or rotor asymmetries)

$$[U_s] = [R_s][I_s] + d[\Psi_s]/dt \tag{1}$$

$$[0] = [R_r][I_r] + d[\Psi_r]/dt \tag{2}$$

$$[\Psi_s] = [L_{ss}][I_s] + [L_{sr}][I_r] \tag{3}$$

$$[\Psi_r] = [L_{sr}]^T[I_s] + [L_{rr}][I_r] \tag{4}$$

$$[U_s] = [u_{s1}, u_{s2}, ...u_{sm}]^T \quad (5)$$

$$[I_s] = [i_{s1}, i_{s2}, ...i_{sm}]^T \quad (6)$$

$$[I_r] = [i_{r1}, i_{r2}, ...i_{rn}]^T \quad (7)$$

where $[U]$ is the phase voltages matrix, $[I]$ is the phase currents matrix, $[R]$ is the resistances matrix, $[\Psi]$ is the flux linkages matrix and $[L]$ is the inductances matrix. Subscripts s and r are used for the stator and for the rotor, respectively. The mechanical equations are:

$$T_e = \frac{1}{2}[I]^T \frac{\partial [L]}{\partial \theta}[I] \quad (8)$$

$$T_e - T_L = J\frac{d\Omega}{dt} = J\frac{d^2\theta}{dt^2} \quad (9)$$

where T_e is the electromechanical torque of the machine, T_L is the load torque, J is the total system inertia (rotor plus load), Ω is the mechanical speed and θ is the mechanical angle position of the rotor. To solve (3), (4) and (8), the self and mutual phase inductance matrices must be calculated for every rotor position. Due to the presence of the derivatives in (1), (2) and (8), it is necessary to achieve a very good accuracy in this process, especially if different fault conditions are to be detected and diagnosed in a sure way. The elements of the matrices L_{SS}, L_{RR} and L_{SR}, are computed in this work using a novel approach based on the FFT, which provides the mutual inductance between two phases for all of their relative angular positions, taking into account the air gap MMF harmonics. End turn and slot leakage inductances need to be pre-calculated, and are included in the L terms in (3) and (4), as usual in the technical literature, where explicit expressions for these inductances can be found in [86–88].

3. Modelling of the Eccentric Air Gap Length

Under the assumption of infinite iron permeability and smooth, constant air gap, the mutual inductances of the phases only change with their relative position [1]. For non uniform air gaps, the relative position between the phases, as well as the rotor position, have to be taken into account. If both the stator and rotor cores are cylindrical, the eccentricity can be fully defined just by the position of the rotor geometric centre, O_r with respect to the stator geometric centre O_s. To analyze the eccentric machine, a coordinate system attached to the stator will be used in this paper, as shown in Fig. 1

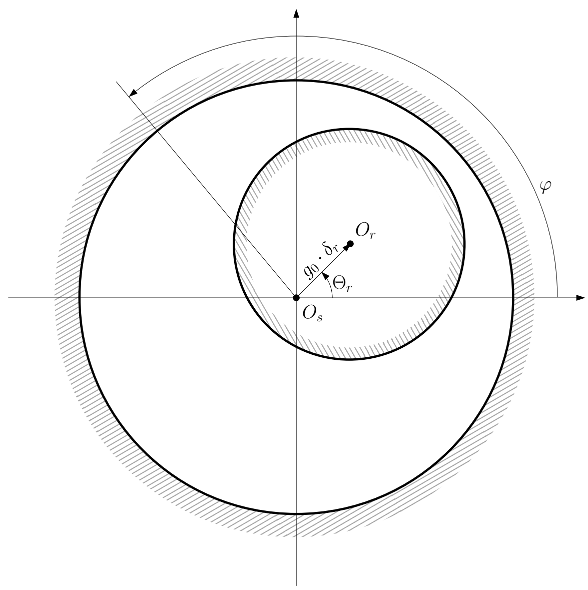

Figure 1: Coordinate system used in this paper, attached to the stator. φ is the angular coordinate of a generic point on the rotor external surface or on the stator internal one. The position of the rotor centre in the eccentric machine, O_r, is given by its angular position, Θ_r, and its distance to the stator centre, δ_r, in p.u. of the air gap length of the healthy machine, g_0. That is, $\overrightarrow{O_sO_r} = g_0 \cdot \delta_r \cdot e^{j\Theta_r}$.

In this coordinate system, the degree of eccentricity can be fully characterized by the position of the rotor centre, shown in detail in Fig. 2

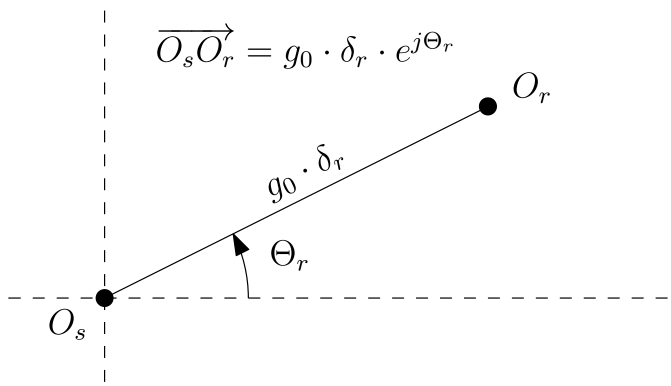

Figure 2: Parameters used for characterizing the degree of eccentricity: distance from the rotor axis to the stator axis ($g_0 \cdot \delta_r$), and angular position of the rotor centre, measured in a stator reference frame (Θ_r).

$$\overrightarrow{O_sO_r} = g_0 \cdot \delta_r \cdot e^{j\Theta_r} \quad 0 \leq \delta_r < 1,\ 0 \leq \Theta_r < 2\pi \tag{10}$$

where g_0 is the air gap width of the healthy machine, δ_r is the distance from the rotor axis to the stator axis (in p.u. of g_0), which is assumed constant along the machine axial length, and Θ_r is the angular position of the rotor centre, measured in a stator reference frame.

Assuming, without any loss of generality, that the rotor centre lies in the stator d-axis, that is, $\Theta_r = 0$ in Fig. 1, the air gap length at an angular position φ, $g(\varphi)$ in Fig. 3, is given by the distance between a point on the external surface of the rotor at this coordinate P_R, and a point on the inner surface of the stator at the same coordinate, P_S. That is,

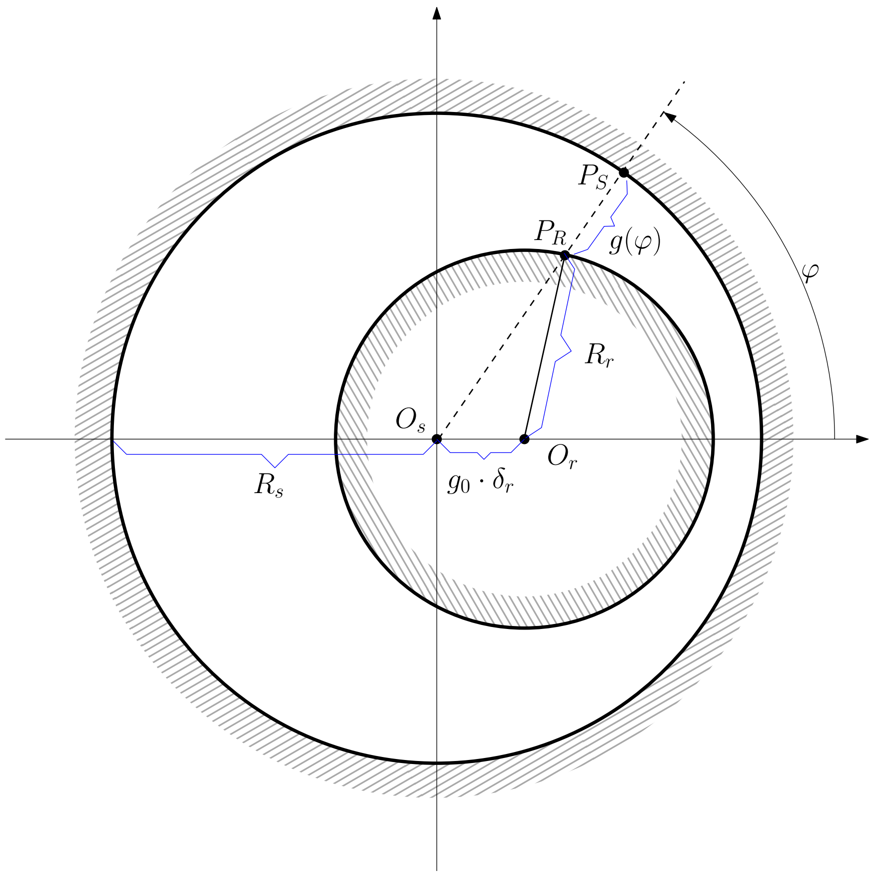

Figure 3: Air gap length $g(\varphi)$ of an eccentric machine as a function of the angular coordinate φ, measured in a stator reference frame.

$$g(\varphi) = |\overline{O_s P_S} - \overline{O_s P_R}| = R_s - |\overline{O_s P_R}| \tag{11}$$

where R_s is the stator radius. The rotor radius, R_r, can be expressed as a function of $\overline{O_s P_R}$ as

$$R_r^2 = |\overline{O_s P_R}|^2 + (g_0 \cdot \delta_r)^2 - 2|\overline{O_s P_R}| \cdot g_0 \cdot \delta_r \cdot \cos(\varphi) \tag{12}$$

that is,

$$|\overline{O_s P_R}| = \frac{2g_0 \cdot \delta_r \cdot \cos(\varphi) \pm \sqrt{(2g_0 \cdot \delta_r \cdot \cos(\varphi))^2 - 4(g_0^2 \cdot {\delta_r}^2 - R_r^2)}}{2} \tag{13}$$

and, substituting (13) in (11) gives

$$g(\varphi) = R_s - g_0 \cdot \delta_r \cos(\varphi) \pm \sqrt{(g_0 \cdot \delta_r \cdot \cos(\varphi))^2 - g_0^2 \cdot {\delta_r}^2 + R_r^2} \tag{14}$$

Assuming that the radius of the rotor is much greater than the air gap length, $R_r >> g_0 \cdot \delta_r$, then (14) becomes

$$g(\varphi) \approx R_s - R_r - g_0 \cdot \delta_r \cos(\varphi)) \approx g_0(1 - \delta_r \cos(\varphi)) \tag{15}$$

From (15), the air gap length at any given angular coordinate φ can be approximated by a function of the rotor centre coordinates δ_r and Θ_r as

$$g(\varphi, \Theta_r, \delta_r) \approx g_0 \cdot (1 - \delta_r \cdot \cos(\varphi - \Theta_r)) \tag{16}$$

3.1. Inverse of the Air-Gap Function

For computing the phases' inductances, it is needed the inverse of the air gap function to obtain the permeance function of the machine. The inverse of (16) is given by

$$g(\varphi, \Theta_r, \delta_r)^{-1} = g_0^{-1} \cdot \frac{1}{(1 - \delta_r \cdot \cos(\varphi - \Theta_r))} \tag{17}$$

The mean air gap radius of the machine, $r(\varphi, \Theta_r, \delta_r)$, can be defined in terms of the stator inner radius R_s and the rotor's outer one, R_r as

$$r(\varphi, \Theta_r, \delta_r) \approx r = \frac{R_s + R_r}{2} \tag{18}$$

Neglecting the variations of the mean air gap radius (18), the function given by (17) can be expressed as the series [89]

$$\frac{1}{1 - \delta_r \cdot \cos(\varphi - \Theta_r)} = \frac{1}{\sqrt{1 - {\delta_r}^2}} + 2\sum_{m=1}^{\infty} \left[\left(\frac{1 - \sqrt{1 - {\delta_r}^2}}{\sqrt{1 - {\delta_r}^2}} \right)^m \cos\Big(m(\varphi - \Theta_r)\Big)) \right] \tag{19}$$

Only the first term of the series in (19) have been used in [90–95] and two terms in [89]. In this paper, the equations are derived for a generic number n_t of terms, where the value of n_t can be freely chosen to achieve the desired precision.

Applying (19) to (17) gives

$$g(\varphi, \Theta_r, \delta_r)^{-1} = g_0^{-1} \cdot \left(A_0 + \sum_{m=1}^{n_t} A_m \cdot \cos\Big(m(\varphi - \Theta_r)\Big) \right) \tag{20}$$

where

$$A_0 = \frac{1}{\sqrt{1 - {\delta_r}^2}} \tag{21}$$

and

$$A_m = 2 \left(\frac{1 - \sqrt{1 - {\delta_r}^2}}{\sqrt{1 - {\delta_r}^2}} \right)^m \qquad m = 1 \ldots n_t \tag{22}$$

4. Yoke Flux Generated by a Single Conductor in an Eccentric Induction Machine

Let's consider a conductor of the eccentric induction machine, placed in the air-gap at a given angular position α (Fig. 4).

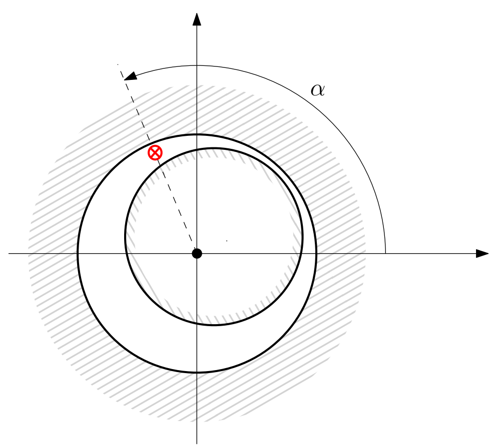

Figure 4: Single conductor of the eccentric induction machine, placed in the air-gap, at a given angular position α.

To obtain the yoke flux distribution that this single conductor generates for any given rotor centre position $\overrightarrow{O_s O_r} = \delta_r \cdot e^{j\Theta_r}$ when it is fed with a unit current, the following steps are taken in this work:

1. The air gap MMF generated by a one-turn, short pitched coil is determined for an eccentric machine, with the rotor centre at the arbitrary

position $\overrightarrow{O_sO_r} = \delta_r \cdot e^{j\Theta_r}$ (Section 4.1).

2. Based on the air gap MMF of a short pitched coil, the air gap MMF of a single conductor is obtained (Section 4.2).
3. From the air gap MMF of the conductor, the magnetic flux density distribution that it generates along the non-uniform air gap of the eccentric machine is obtained (Section 4.3).
4. Finally, the yoke flux generated by the conductor is calculated, based on its MMF (Section 4.4).

Using the yoke flux of this single conductor in the eccentric machine's airgap, the convolution theorem will be used in Section 6, first, to compute the yoke flux produced by an arbitrary phase A, and, thereafter, the flux linkage of a phase B due to phase A, for any position of the rotor and any relative position of both phases.

4.1. Air Gap MMF Generated by a One-turn, Short Pitched Coil in an Eccentric Induction Machine

The air gap MMF generated by a coil along the air gap of an eccentric induction machine at an angular coordinate φ, $F_c(\varphi, \Theta_r, \delta_r)$, is given by the relation

$$F_c(\varphi, \Theta_r, \delta_r) = H_c(\varphi, \Theta_r, \delta_r) \cdot g(\varphi, \Theta_r, \delta_r) \tag{23}$$

where φ is the angular coordinate, $\overrightarrow{O_sO_r} = g_0 \cdot \delta_r \cdot e^{j\Theta_r}$ is the position of the rotor geometric centre, $H_c(\varphi, \Theta_r, \delta_r)$ is the mean value of the radial component of the magnetic field intensity at φ and $g(\varphi, \Theta_r, \delta_r)$ is the air gap length at the angular coordinate φ. Let's consider the general case of a short-pitched, one-turn coil, with its first conductor placed at the origin $\varphi = 0$, and the other one at position $\varphi = \alpha$ (see Fig. 5a), fed with a unit current, and with the rotor centre placed at the arbitrary position $\overrightarrow{O_sO_r} = g_0 \cdot \delta_r \cdot e^{j\Theta_r}$. The air gap MMF generated by this coil at a generic coordinate φ, $F_{0\alpha}(\varphi, \Theta_r, \delta_r)$, can be calculated applying Ampere's law to a path as the one labelled '*abcd*' in Fig. 5, under the assumption of infinite iron permeability, straight conductors and uniform air gap length along the machine axis, in the z direction.

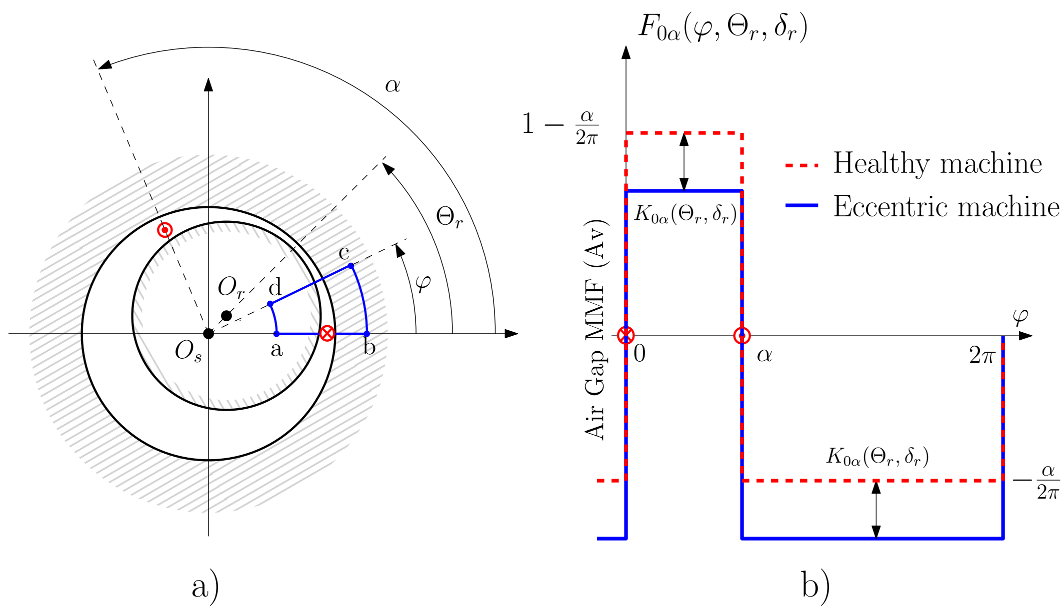

Figure 5: a) Short pitched coil fed by a dc current of 1 A. b) MMF generated by a short pitched coil $F_{0\alpha}(\varphi, \Theta_r, \delta_r)$ in a healthy machine (red, dashed line) and in an eccentric induction machine (blue, solid line), as a function of the angular coordinate φ, and of the position of the rotor centre $\overrightarrow{O_sO_r} = g_0 \cdot \delta_r \cdot e^{j\Theta_r}$.

$$\begin{cases} F_{0\alpha}(\varphi, \Theta_r, \delta_r) - F_{0\alpha}(0, \Theta_r, \delta_r) = 1 & 0 \leq \varphi < \alpha \\ F_{0\alpha}(\varphi, \Theta_r, \delta_r) - F_{0\alpha}(0, \Theta_r, \delta_r) = 0 & \alpha \leq \varphi < 2\pi \end{cases} \tag{24}$$

The total flux crossing a cylindrical surface of radius r and unit length, parallel to the stator bore axis, amounts to zero. Therefore

$$\mu_0 \cdot r \cdot \int_0^{2\pi} H_c(\varphi, \Theta_r, \delta_r) \cdot d\varphi = 0 \tag{25}$$

and, taking into account (23) and (24), (25) gives

$$\int_0^{\alpha} \frac{(1 + F_{0\alpha}(0, \Theta_r, \delta_r))}{g(\varphi, \Theta_r, \delta_r)} d\varphi + \int_{\alpha}^{2\pi} \frac{F_{0\alpha}(0, \Theta_r, \delta_r)}{g(\varphi, \Theta_r, \delta_r)} d\varphi = 0 \tag{26}$$

that is,

$$F_{0\alpha}(0, \Theta_r, \delta_r) = -\frac{\int_0^{\alpha} g(\varphi, \Theta_r, \delta_r)^{-1} d\varphi}{\int_0^{2\pi} g(\varphi, \Theta_r, \delta_r)^{-1} d\varphi} \tag{27}$$

Replacing (20) in (27) gives

$$F_{0\alpha}(0, \Theta_r, \delta_r) = -\frac{\alpha}{2\pi} - \sum_{m=1}^{n_t} \frac{A_m}{2\pi A_0} \frac{\sin(m\Theta_r) - \sin(m(\Theta_r - \alpha))}{m} \tag{28}$$

and, combining (28) and (24), gives finally

$$F_{0\alpha}(\varphi, \Theta_r, \delta_r) = \begin{cases} 1 - \frac{\alpha}{2\pi} - \sum_{m=1}^{n_t} \frac{A_m}{2\pi A_0} \frac{\sin(m\Theta_r) - \sin(m(\Theta_r - \alpha))}{m} & 0 \leq \varphi < \alpha \\ -\frac{\alpha}{2\pi} - \sum_{m=1}^{n_t} \frac{A_m}{2\pi A_0} \frac{\sin(m\Theta_r) - \sin(m(\Theta_r - \alpha))}{m} & \alpha \leq \varphi < 2\pi \end{cases} \tag{29}$$

that is

$$F_{0\alpha}(\varphi, \Theta_r, \delta_r) = \begin{cases} 1 - \frac{\alpha}{2\pi} - K_{0\alpha}(\Theta_r, \delta_r) & 0 \leq \varphi < \alpha \\ -\frac{\alpha}{2\pi} - K_{0\alpha}(\Theta_r, \delta_r) & \alpha \leq \varphi < 2\pi \end{cases} \tag{30}$$

with

$$K_{0\alpha}(\Theta_r, \delta_r) = \sum_{m=1}^{n_t} \frac{A_m}{2\pi A_0} \frac{\sin(m\Theta_r) - \sin(m(\Theta_r - \alpha))}{m} \tag{31}$$

It should be noted that the expression of the MMF generated by a short pitched coil of a healthy (non-eccentric) IM [82, 96] can be deduced as a particular case of (30) in which $\delta_r = 0$ (and, therefore $K_{0\alpha}(\Theta_r, \delta_r) = 0$); Fig. 5.b shows the waves of MMF of the short pitched coil in a healthy machine (red line) and in eccentric one (blue line). It is remarkable that the MMF wave of the eccentric machine can be obtained shifting down the wave of the healthy machine a distance $K_{0\alpha}$, that only depends on the rotor centre position.

4.2. Air Gap MMF Generated by a Single Conductor in an Eccentric Induction Machine

The MMF generated by the short pitched coil (29) can be expressed also as the sum of the MMFs generated by each of its conductors, taking into account the opposite direction of their currents, that is

$$F_{0\alpha}(\varphi, \Theta_r, \delta_r) = F_0(\varphi, \Theta_r, \delta_r) - F_\alpha(\varphi, \Theta_r, \delta_r) \tag{32}$$

A close inspection of (29) shows the presence of two terms in the summation, each of them corresponding to one of the coil's conductors:

- One of them is proportional to $\sin(m\Theta_r)$, which can be attributed to the MMF of the conductor placed at the origin $\varphi = 0$
- The other one is proportional to $-\sin(m(\Theta_r - \alpha))$, which can be attributed the MMF of the conductor placed at $\varphi = \alpha$, with the sign reversed to account for the direction of the current.

Therefore, the expression of the MMF of a single conductor placed at an angular position α in the eccentric machine, $F_\alpha(\varphi, \Theta_r, \delta_r)$, which satisfies (32), can be expressed as

$$F_\alpha(\varphi, \Theta_r, \delta_r) = \begin{cases} \frac{1}{2} - \frac{(\varphi-\alpha)}{2\pi} - K_\alpha(\Theta_r, \delta_r) & 0 \le \varphi < \alpha \\ -\frac{1}{2} - \frac{(\varphi-\alpha)}{2\pi} - K_\alpha(\Theta_r, \delta_r) & \alpha \le \varphi < 2\pi \end{cases} \tag{33}$$

with

$$K_\alpha(\Theta_r, \delta_r) = \sum_{m=1}^{n_t} \frac{A_m}{2\pi A_0} \frac{\sin(m(\Theta_r - \alpha))}{m} \tag{34}$$

Fig. 6.b shows the spatial wave of MMF generated by the single conductor shown in Fig. 6.a. The red line corresponds to the healthy machine, obtained for δ_r=0, $K_\alpha(\Theta_r, \delta_r)$=0 in (33). The blue line corresponds to an eccentric machine ($K_\alpha(\Theta_r, \delta_r) \neq 0$ in (33)). It is noticeable that, similarly to the case of a short pitched coil, the MMF wave generated by a conductor in the eccentric machine can be obtained by shifting down the MMF corresponding to a healthy machine a distance K_α, which depends on the rotor centre position. Furthermore, it should be noted that the expression of the MMF generated by a single conductor of a healthy, non-eccentric IM [82, 96, 97] can be deduced as a particular case of (33) in which $\delta_r = 0$ (and, therefore, $K_\alpha = 0$).

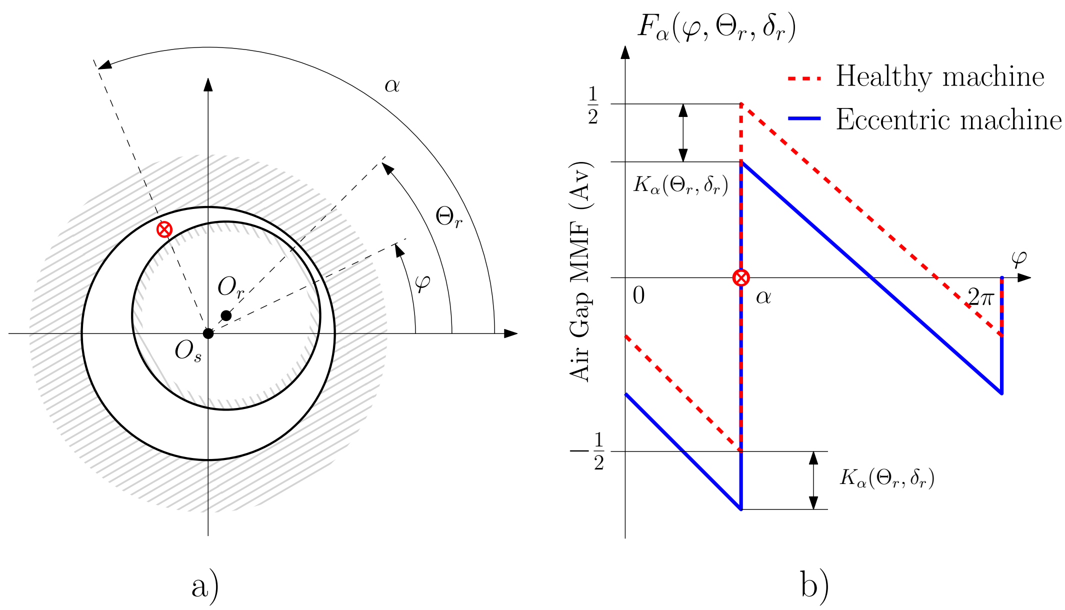

Figure 6: a) Single conductor, placed at an angular position α, fed by a dc current of 1 A. b) MMF generated by a single conductor placed at an angular position α, $F_\alpha(\varphi, \Theta_r, \delta_r)$, in a healthy machine (red, dashed line) and in an eccentric induction machine (blue, solid line), as a function of the angular coordinate φ, and of the position of the rotor centre $\overrightarrow{O_s O_r} = g_0 \cdot \delta_r \cdot e^{j\Theta_r}$.

Eq. (37) can be expressed in a more compact way by wrapping the angular coordinates to the interval $[0, 2\pi)$,

$$F_\alpha(\varphi, \Theta_r, \delta_r) = \frac{1}{2} - \frac{((\varphi - \alpha))_{2\pi}}{2\pi} - K_\alpha(\Theta_r, \delta_r) \tag{35}$$

where $((\varphi - \alpha))_{2\pi}$ stands for the modulo 2π operation

$$((\varphi - \alpha))_{2\pi} = \quad \mathrm{mod}\Big((\varphi - \alpha + 2\pi), 2\pi\Big) \tag{36}$$

For easy of notation, in the rest of this paper the modulo notation will be omitted, and all the angular variables will be assumed to be wrapped to the $[0, 2\pi)$ range, so that (35) will be written as

$$F_\alpha(\varphi, \Theta_r, \delta_r) = \frac{1}{2} - \frac{(\varphi - \alpha)}{2\pi} - K_\alpha(\Theta_r, \delta_r) \tag{37}$$

Without eccentricity, $K_\alpha(\Theta_r, \delta_r) = 0$ and (37) reduces to

$$F_\alpha(\varphi) = \frac{1}{2} - \frac{(\varphi - \alpha)}{2\pi} \tag{38}$$

which is the air gap MMF generated by a conductor placed at an angular position α in a non-eccentric induction machine [82, 96, 97], as shown in Fig 6b, red line.

It is worth mentioning that the air gap MMF of an arbitrary coil (e.g. a short-pitched coil) obtained by Ampere's Law, coincides with the one given by summing up the air gap MMFs of its conductors, computed through (37). Therefore, the air gap MMF of an arbitrary phase can be expressed as the sum of the air gap MMFs of all of its conductors. Fig. 7 shows a simple case with a phase formed by a one-turn, short-pitched coil.

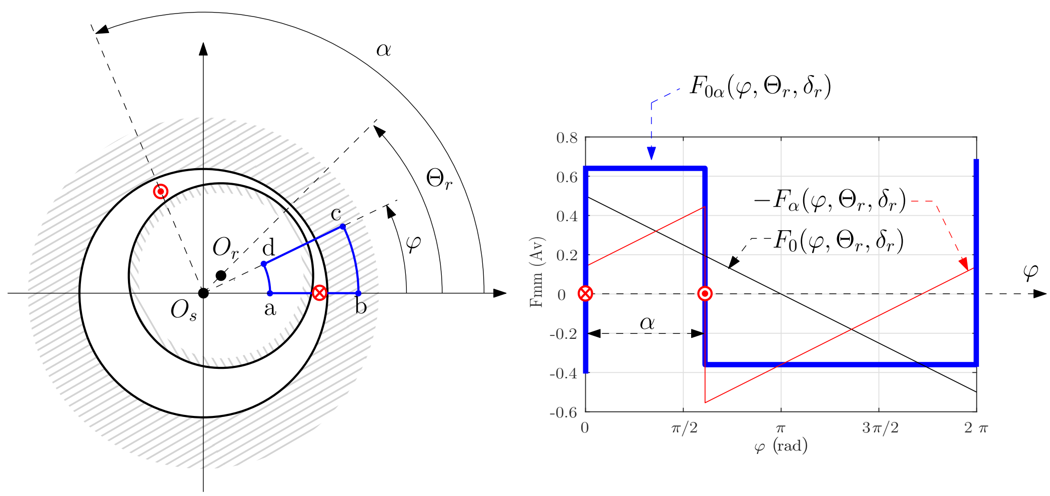

Figure 7: Air gap MMF generated by a one-turn short pitched coil, fed with a unit current, as the sum of the air gap MMFs of both conductors in the eccentric induction machine of Appendix A, for $\delta_r = 0.6$ and $\Theta_r = 0$.

4.3. Magnetic Flux Density of a Single Conductor in an Eccentric Induction Machine

The radial component of the magnetic flux density, or magnetic induction B, at a point of angular coordinate φ, located at the inner surface of the stator bore, that generates a single conductor placed at an angular position

α, fed with a unit current, is given by

$$B_\alpha(\varphi, \Theta_r, \delta_r) = \mu_0 \cdot \frac{F_\alpha(\varphi, \Theta_r, \delta_r)}{g(\varphi, \Theta_r, \delta_r)} \tag{39}$$

and, replacing (20) and (37) in (39), gives

$$\begin{aligned} B_\alpha(\varphi, \Theta_r, \delta_r) = \ & \mu_0 \cdot g_0^{-1} \cdot \left(\tfrac{1}{2} - \tfrac{(\varphi - \alpha)}{2\pi} - K_\alpha(\Theta_r, \delta_r) \right) \cdot \\ & \cdot \left(A_0 + \sum_{m=1}^{n_t} A_m \cdot \cos\left(m(\varphi - \Theta_r) \right) \right) \end{aligned} \tag{40}$$

As in the case of the air gap MMF, the magnetic flux density generated by an arbitrary phase can be expressed as the sum of the magnetic flux density generated by all of its conductors. Fig. 8 shows a simple case with a phase formed by a one-turn, short-pitched coil.

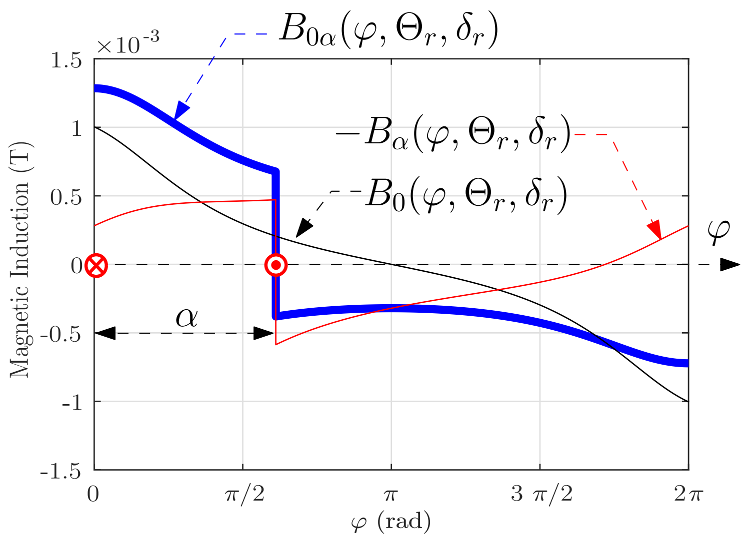

Figure 8: Magnetic flux density generated by a one-turn short pitched coil, fed with a unit current, as the sum of the magnetic flux density of both conductors, in the eccentric induction machine of Appendix A, for $\delta_r = 0.6$ and $\Theta_r = 0$.

4.4. Yoke Flux of a Single Conductor in an Eccentric Induction Machine

If the conductor is placed at an angular position α and fed with a unit current, the differential of the magnetic flux due to the conductor which crosses the corresponding air-gap at an angle φ, for a given position of the rotor centre, $\overrightarrow{O_s O_r} = g_0 \cdot \delta_r \cdot e^{j\Theta_r}$, is (Fig. 9)

$$d\left(\Phi_\alpha(\varphi, \Theta_r, \delta_r)\right) = \Phi_\alpha(\varphi + d\varphi, \Theta_r, \delta_r) - \Phi_\alpha(\varphi, \Theta_r, \delta_r) \tag{41}$$

It can be expressed as a function of the induction's radial component, as in [82] (see Fig. 9)

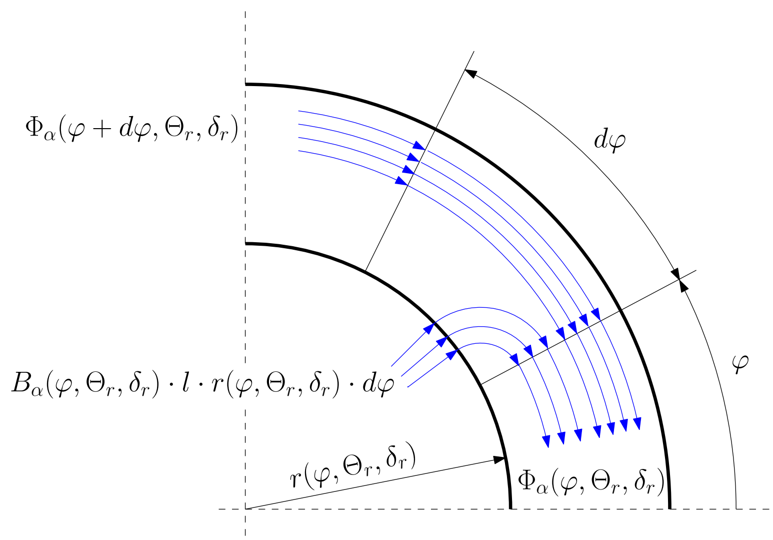

Figure 9: Differential of the yoke flux as a function of the radial component of the induction on the stator inner surface.

$$d\left(\Phi_\alpha(\varphi, \Theta_r, \delta_r)\right) = -B_\alpha(\varphi, \Theta_r, \delta_r) \cdot l \cdot r(\varphi, \Theta_r, \delta_r) \cdot d\varphi \tag{42}$$

where l is the axial length of the stator bore. As the air-gap width is considered to be very small, the radius $r(\varphi, \Theta_r, \delta_r)$ can be approximated by its mean value $r(\varphi, \Theta_r, \delta_r)$, given by (18), as done in [90, 94, 95]. The substitution of (18), (39) and (20) in (42) yields

$$\begin{aligned} d\left(\Phi_\alpha(\varphi, \Theta_r, \delta_r)\right) = \ & -\tfrac{\mu_0 l r}{g_0} \left(\tfrac{1}{2} - \tfrac{(\varphi - \alpha)}{2\pi} - K_\alpha(\Theta_r, \delta_r)\right) \cdot \\ & \cdot \left(A_0 + \sum_{m=1}^{n_t} A_m \cos\left(m(\varphi - \Theta_r)\right)\right) d\varphi \end{aligned} \tag{43}$$

Equation (43) is integrated, which gives

$$\Phi_\alpha(\varphi, \Theta_r, \delta_r) = \frac{\mu_0 l r}{g_0} \cdot \Lambda_\alpha(\varphi, \Theta_r, \delta_r)) + C \tag{44}$$

with

$$\Lambda_\alpha(\varphi, \Theta_r, \delta_r) = \tfrac{A_0}{4\pi}(\varphi-\alpha)^2 + \sum_{m=1}^{n_t} \tfrac{A_m}{2\pi} \left(\frac{(\varphi-\alpha)\sin\Big(m(\varphi-\Theta_r)\Big)}{m} + \frac{\cos\Big(m(\varphi-\Theta_r)\Big)}{m^2} \right) - \\ \left(\tfrac{1}{2} - K_\alpha(\Theta_r, \delta_r)\right) \cdot \left(A_0(\varphi-\alpha) + \sum_{m=1}^{n_t} A_m \frac{\sin\Big(m(\varphi-\Theta_r)\Big)}{m} \right) \tag{45}$$

The value of constant C in (44) is given by the condition that, due to the cyclic nature of the yoke flux generated by a single conductor, its minimum value is set to zero. Besides, $\Lambda_\alpha(\varphi, \Theta_r, \delta_r)$ depends only on the degree of eccentricity, and is independent of the geometric parameters of the machine. Therefore, it needs to be evaluated only once, and it is scaled to any given machine using the scaling factor $\frac{\mu_0 l r}{g_0}$.

As in the case of the magnetic flux density, the yoke flux generated by an arbitrary phase can be expressed as the sum of the yoke flux generated by all of its conductors. Fig. 10 shows a simple case with a phase formed by a one-turn, short-pitched coil.

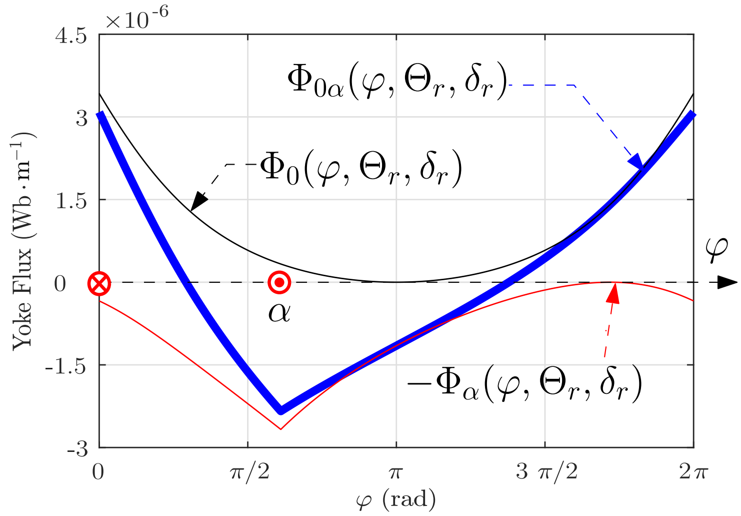

Figure 10: Yoke flux generated a one-turn short pitched coil, fed with a unit current, as the sum of the magnetic flux density of both conductors, in the eccentric induction machine of Appendix A, for $\delta_r = 0.6$ and $\Theta_r = 0$.

5. Position of the Rotor centre as a Function of the Type and Degree of Eccentricity

Eq. (44) gives the yoke flux generated by a single conductor of an eccentric machine as a function of the rotor centre coordinates, Θ_r and δ_r. But, when the rotor turns around it rotation centre by an angle $\theta_r(t)$, it is necessary to obtain an expression that gives the coordinates of the rotor centre as a function of the rotor angular position $\theta_r(t)$. Such an expression is derived in this section, and depends on the type of rotor eccentricity. Three cases will be analyzed in this paper: static eccentricity (SE), dynamic eccentricity (DE) and mixed eccentricity (ME). Other types of eccentricity, such as axial [60], inclined [98] or curved eccentricity [59, 78], are outside the scope of this paper.

5.1. Static Eccentricity

SE is characterized (Fig. 11) by a displacement of the axis of rotation of the rotor (O_r) with respect to the geometric centre of the stator (O_s). The axis of rotation of the rotor O_θ coincides with the rotor geometrical centre. It can be caused by misalignments of the mounted bearings, or of the bearing plates. The rotor is not centreed with the stator bore, but it rotates around its geometric centre (46), that is, Θ_r= constant. In the case of static eccentricity, it will assumed in this work, without any of loss of generality, that the rotor centre lies in the stator d-axis (Θ_r=0). Therefore, (10) becomes

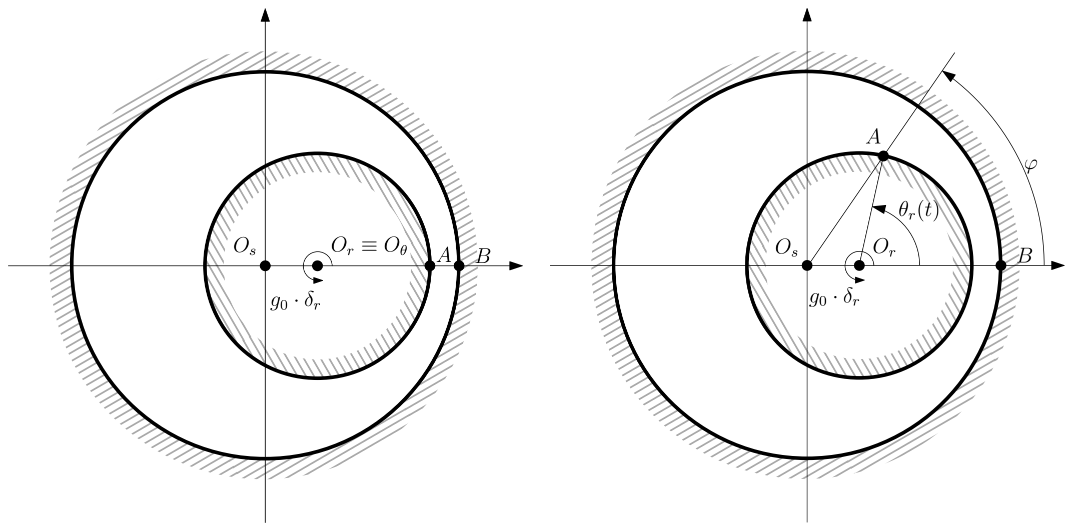

Figure 11: Static eccentricity. Relative position of a rotor conductor, A, and a stator conductor, B, when the rotor turns an angle $\theta_r(t)$ (right) from the initial line (left), in the case of SE. The minimum air gap length is always located at the position of the stator conductor B.

$$\overrightarrow{O_sO_r} = g_0 \cdot \delta_r \tag{46}$$

The air gap length is non uniform, but its shape does not change when the rotor turns (Fig. 11). Therefore, self and mutual inductances of the stator windings, $\mathbf{L_{ss}}$ in (3), are constant, whereas self and mutual inductances of the rotor windings, $\mathbf{L_{rr}}$ in (4), and mutual inductances between stator and rotor windings, $\mathbf{L_{sr}}$ in (3), (4) and (8), change when the rotor turns.

5.2. Dynamic Eccentricity

DE is characterized (Fig. 12) by a displacement of the rotor geometric centre (O_r) from its rotating axis (O_θ), which coincides with the stator bore axis (O_s). It may be caused by a manufacturing defect, a bent shaft, bearings defects, etc. Under DE, the rotor centre spins along a circular path with the same speed as the rotor does. In this case, (10) becomes (47),

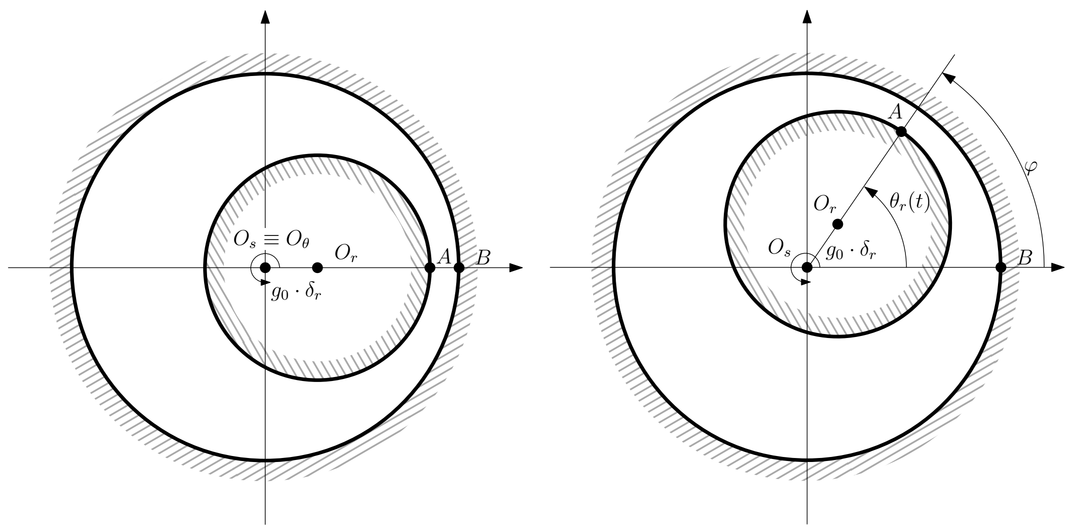

Figure 12: Dynamic eccentricity. Relative position of a rotor conductor, A, and a stator conductor, B, when the rotor turns an angle $\theta_r(t)$ (right) from the initial line (left), in the case of DE. The minimum air-gap length is always located at the position of the rotor conductor A.

$$\overrightarrow{O_sO_r} = g_0 \cdot \delta_r \cdot e^{j\theta_r} \tag{47}$$

where θ_r stands for the angle position of the rotor centre in stator coordinates. In this case, the position of the minimum air gap rotates with the rotor (Fig. 12), so that, contrary to the SE case, self and mutual inductances of the stator windings ($\mathbf{L_{ss}}$), and mutual inductances between stator and rotor windings ($\mathbf{L_{sr}}$) change when the rotor turns, whereas self and mutual inductances between rotor windings ($\mathbf{L_{rr}}$) are not affected by the rotation of the machine.

5.3. Mixed Eccentricity

ME appears when both SE and DE are present. In this case , the rotating axis (O_θ in Fig. 13) is displaced both from the stator geometric centre (O_s) and from the rotor centre (O_r). From Fig. 13 and (10), the position of the rotor centre can be expressed as a function of the degree of static eccentricity (δ_{se}) and the degree of dynamic eccentricity (δ_{de}) as

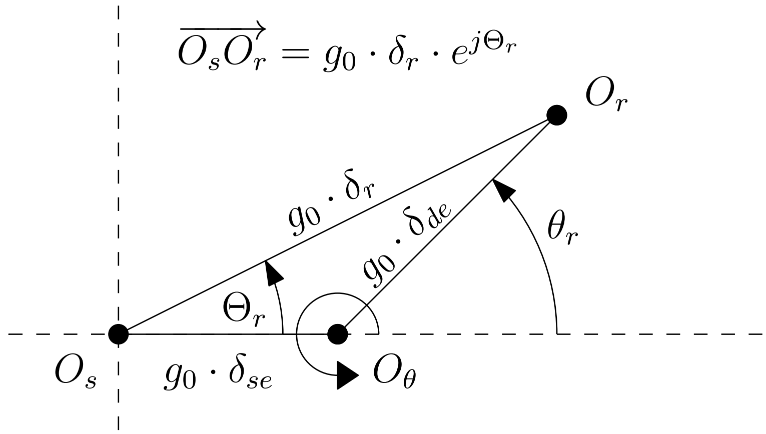

Figure 13: Mixed eccentricity. Position of the rotor geometric centre (O_r) in a system of coordinates fixed to the stator, in case of ME.

$$\overrightarrow{O_sO_r} = \overrightarrow{O_sO_\theta} + \overrightarrow{O_\theta O_r} = g_0 \cdot (\delta_{se} + \delta_{de} \cdot e^{j\theta_r}) = g_0 \cdot \delta_r \cdot e^{j\Theta_r} \tag{48}$$

with

$$\delta_r = \sqrt{{\delta_{se}}^2 + {\delta_{de}}^2 + 2 \cdot \delta_{se} \cdot \delta_{de} \cdot \cos(\theta_r)} \tag{49}$$

and

$$\Theta_r = \tan^{-1}\left(\frac{\delta_{de} \cdot \sin(\theta_r)}{\delta_{se} + \delta_{de} \cdot \cos(\theta_r)}\right) \tag{50}$$

The expressions for SE and DE, given by (46) and (47) can be considered as particular cases of (48), as shown in Fig. 14 and in Table 1.

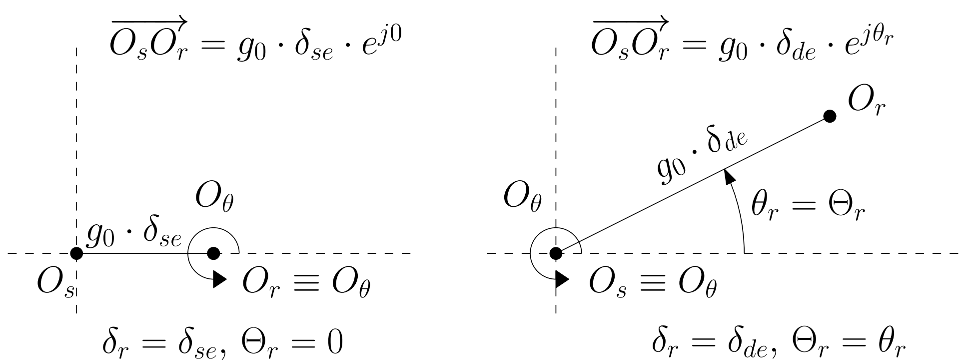

Figure 14: Position of the rotor geometric centre (O_r) in a system of coordinates fixed to the stator, in case of static eccentricity (left) and dynamic eccentricity (right).

Table 1: Types of rotor eccentricity

Type	δ_r	Θ_r
SE	δ_{se}	0
DE	δ_{de}	θ_r
ME	$\sqrt{{\delta_{se}}^2 + {\delta_{de}}^2 + 2 \cdot \delta_{se} \cdot \delta_{de} \cdot \cos(\theta_r)}$	$\tan^{-1}\left(\frac{\delta_{de} \cdot \sin(\theta_r)}{\delta_{se} + \delta_{de} \cdot \cos(\theta_r)}\right)$

Therefore, the loci of the positions of the geometric rotor centre in a reference system fixed to the stator defines the type of eccentricity, as seen in Fig. 15. In the case of a healthy machine (Fig. 15.a), the rotor centre is located on the stator geometric centre. In the case of SE (Fig. 15.b), the rotor centre is placed in a fixed position, different from the stator centre. In the case of DE, the rotor centre describes a circumference centred in the stator centre (Fig. 15.c). Finally, in the ME case, the rotor centre describes a circumference whose centre does not coincide with the stator centre ($\delta_r \neq$ const., $\Theta_r \neq$ const.).

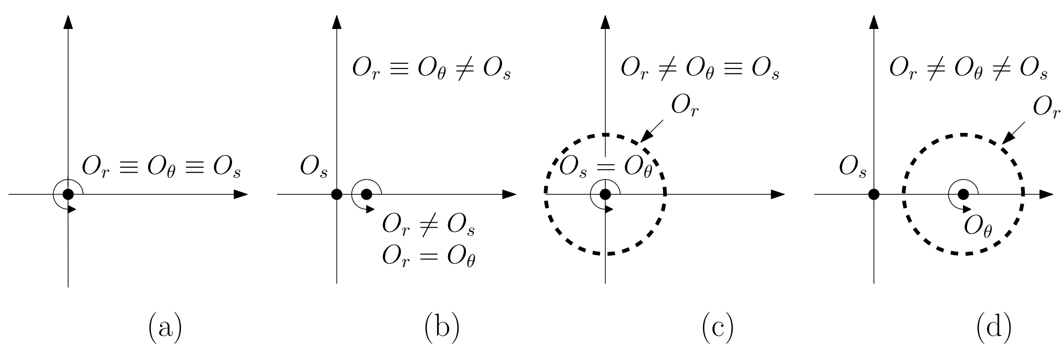

Figure 15: Loci of the positions of the rotor geometric centre (O_r) in a system of coordinates fixed to the stator, in case of (a) healthy machine, (b) static eccentricity, (c) dynamic eccentricity and (d) mixed eccentricity.

In this paper, the most general case, (10), will be analyzed, and the result will be applied to each particular type of eccentricity following (48). The election of the position of the rotor centre as the variable that characterizes the eccentricity is the key point that enables this unified approach.

6. Phases Inductances in an Eccentric Induction Machine

For the simulation of an eccentric induction machine with a given degree of static (δ_{se}) and dynamic (δ_{de}) eccentricity, it is necessary to obtain the phase inductances matrix for each rotor position, θ_r. The goal of this section is to obtain the mutual inductance between two phases of the eccentric machine as a function of their angular positions, for a given position of the rotor. To achieve this goal, it is advisable to express the yoke flux generated by a single conductor as a function of three variables, $\Phi_{cond}(\varphi, \alpha, \theta_r)$, where φ is the angular position where the yoke flux is computed, α is the conductor angular coordinate, and θ_r defines the rotor position. This function can be derived from (44), making use of (49) and (50), as

$$\Phi_{cond}(\varphi, \alpha, \theta_r) = \Phi_\alpha\Big(\varphi, \Theta_r(\theta_r), \delta_r(\theta_r)\Big) = \Phi_\alpha(\varphi, \theta_r) \tag{51}$$

since, for a given degree of SE (δ_{se}) and DE (δ_{de}), the coordinates of the rotor center Θ_r (50) and δ_r (49) depend only on the rotor position θ_r as

$$\Theta_r(\theta_r) = \tan^{-1}\Big(\frac{\delta_{de}\sin(\theta_r)}{\delta_{se} + \delta_{de}\cos(\theta_r)}\Big) \tag{52}$$

and

$$\delta_r(\theta_r) = \sqrt{{\delta_{se}}^2 + {\delta_{de}}^2 + 2\delta_{se}\delta_{de}\cos(\theta_r)} \tag{53}$$

6.1. Yoke Flux Generated by a Phase in an Eccentric Induction Machine

Let's consider a phase A, with an arbitrary distribution of conductors $Z_A(\alpha)$, $0 \le \alpha < 2\pi$, where $Z_A(\alpha)$ is the number of conductors of phase A on the air gap at angular coordinate α. The yoke flux Φ_A that this phase generates when it is fed with a unit current, and shifted a given angle φ_A, can be obtained as a linear superposition of the yoke flux generated by all of the phase's conductors, (51), as

$$\Phi_A(\varphi, \varphi_A, \theta_r) = \int_0^{2\pi} \Phi_{cond}(\varphi, \alpha, \theta_r)\cdot Z_A(\alpha - \varphi_A)\cdot d\alpha \tag{54}$$

6.2. Flux Linkages of a Phase in an Eccentric Induction Machine

Let's consider now a second phase B, with an arbitrary distribution of conductors $Z_B(\beta)$, $0 \le \beta < 2\pi$. The flux linkages of phase Ψ_B, due to the yoke flux generated by phase A, for any given angular position of phases A and B, can be obtained just by adding the values of the yoke flux generated by phase A at the yoke sections corresponding to each one of the conductors of phase B. Fig. 16 shows the basis of this method: the flux linkage of an arbitrary coil (a, b) can be calculated by replacing the coil by two equivalent annular coils, (a, a') and (b, b'), and summing up the yoke flux that crosses them, $\Phi(\varphi_a)$ and $\Phi(\varphi_b)$.

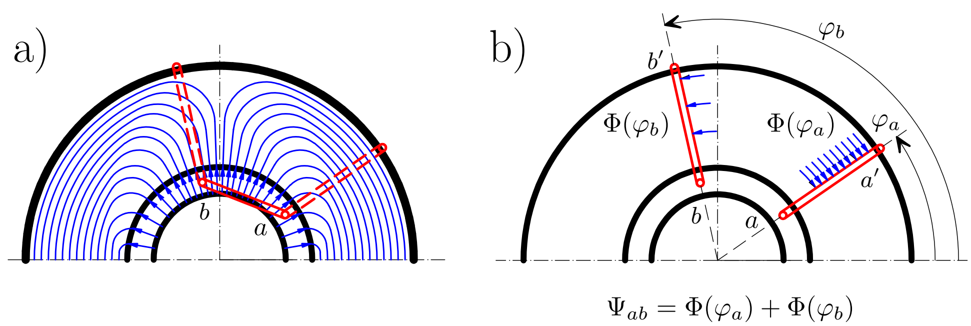

Figure 16: Flux linkage of a single turn coil. a) Actual coil. b) Replaced by two equivalent annular coils.

Following the proposed method, the flux linkages of phase B due to the yoke flux generated by phase A is given by

$$\Psi_{BA}(\varphi_B, \varphi_A, \theta_r) = \int_0^{2\pi} Z_B(\beta - \varphi_B) \cdot \Phi_A(\varphi, \varphi_A, \theta_r)\, d\beta \tag{55}$$

and, combining (54) and (55) gives

$$\Psi_{BA}(\varphi_B, \varphi_A, \theta_r) = \int_0^{2\pi} \int_0^{2\pi} Z_B(\beta - \varphi_B) \cdot \Phi_{cond}(\beta, \alpha, \theta_r) \cdot Z_A(\alpha - \varphi_A) \cdot d\alpha\, d\beta \tag{56}$$

As phase A is fed with a unit current, (56) provides the mutual inductance between phases A and B as a function of their angular positions, for a given rotor position

$$L_{BA}(\varphi_B, \varphi_A, \theta_r) = \int_0^{2\pi} \int_0^{2\pi} Z_B(\beta - \varphi_B) \cdot \Phi_{cond}(\beta, \alpha, \theta_r) \cdot Z_A(\alpha - \varphi_A) \cdot d\alpha\, d\beta \tag{57}$$

From (51) and (57) it holds that

$$L_{BA}(\varphi_B, \varphi_A, \theta_r) = L_{AB}(\varphi_A, \varphi_B, \theta_r) \tag{58}$$

7. Numerical Computation of the Phases Inductances in an Eccentric Induction Machine using the FFT

The computation of (57) can be cumbersome, because a double integral must be computed for obtaining the mutual inductance between two phases A and B for each angular displacement between them, and for every position of the rotor. In this section a novel procedure will be applied to simplify this calculation using the FFT. For the numerical computation of (57), the air gap circumference is divided into N equally spaced angular intervals, with a spatial resolution for the angular coordinate $\Delta\varphi = 2\pi/N$. With this discretization, the functions in (57), defined in this discrete mesh, are converted into the following matrices:

$\mathbf{\Phi_{cond}}$ Yoke flux distribution produced by a single conductor ($\Phi_{cond}(\varphi, \alpha, \theta_r) \rightarrow \mathbf{\Phi_{cond}}[i, j, k]$, with dimension $N \times N \times N$).

The element [i,j,k] of the 3D matrix $\mathbf{\Phi_{cond}}$ (59) contains the yoke flux

- at a generic point of the airgap with an angular coordinate $i \cdot \Delta\varphi$,
- generated by a single conductor, fed with a unit current, placed at an angular position $j \cdot \Delta\varphi$,
- for an angular rotor position equal to $k \cdot \Delta\varphi$.

The 3D matrix $\mathbf{\Phi_{cond}}$ is computed, using (51), as

$$\mathbf{\Phi_{cond}}[i, j, k] = \Phi_{cond}(i\Delta\varphi, j\Delta\varphi, k\Delta\varphi) \;\; \text{with} \;\; i, j, k = 0, 1, \ldots, N-1 \tag{59}$$

$\mathbf{Z_A}$ Distribution of conductors of phase A ($Z_A(\alpha) \rightarrow \mathbf{Z_A}[i]$, with dimension $N \times 1$) The element [i] of the 1D matrix $\mathbf{Z_A}$ (60) contains the number of conductors of phase A at an angular position $i \cdot \Delta\varphi$. The position of phase A axis is considered to be aligned with the stator d-axis, for fixing a common reference frame in the calculation process.

$$\mathbf{Z_A}[i] = Z_A(i\Delta\varphi) \;\; \text{with} \;\; i = 0, 1, \ldots, N-1 \tag{60}$$

$\mathbf{Z_B}$ Distribution of conductors of phase B ($Z_B(\beta) \rightarrow \mathbf{Z_B}[i]$, with dimension $N \times 1$) The element [i] of the 1D matrix $\mathbf{Z_B}$ (61) contains the number of conductors of phase B at an angular position $i \cdot \Delta\varphi$. The position of phase B axis is also considered to be aligned with the stator d-axis.

$$\mathbf{Z_B}[i] = Z_B(i\Delta\varphi) \text{ with } i = 0, 1, \ldots, N-1 \tag{61}$$

$\mathbf{L_{BA}}$ Mutual inductance of phases B and A ($L_{BA}(\varphi_B, \varphi_A, \theta_r) \to \mathbf{L_{BA}}[i, j, k]$, with dimension $N \times N \times N$)

The element [i,j,k] of the 3D matrix $\mathbf{L_{BA}}$ contains the mutual inductance between phases B and A when

- phase B is placed at an angular position $i \cdot \Delta\varphi$,
- phase A is placed at an angular position $j \cdot \Delta\varphi$,
- the rotor centre is placed at an angular position $k \cdot \Delta\varphi$.

These four matrices have been represented in Fig. 17.

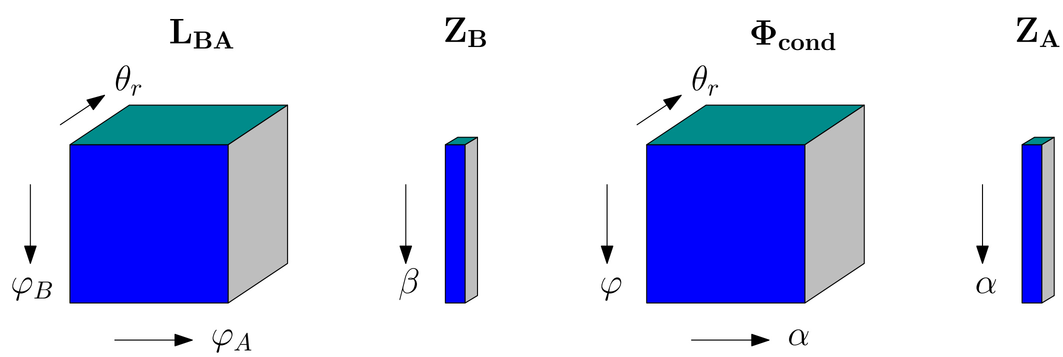

Figure 17: Matrices used for computing the mutual inductance between phases B and A, $\mathbf{L_{BA}}$, for every angular position of phase B, φ_B, of phase A, φ_A, and of the rotor θ_r.

The 3D matrix $\mathbf{L_{BA}}$, which contains the mutual inductances between phases B, and A, for all of their different N possible positions, and for the N different positions of the rotor (N^3 elements), can be computed in a very simple and effective way, making use of the properties of the fast Fourier transform (FFT), and its inverse (IFFT), as

$$\mathbf{L_{BA}} = \text{IFFT}\Big\{ \Big((\text{FFT}\{\mathbf{Z_A}\})' \, * \, \text{FFT}\{\mathbf{\Phi_{cond}}\} \, * \, \text{FFT}\{\mathbf{Z_B}\} \Big) \Big\} \tag{62}$$

where the symbol ' stands for the non-conjugate matrix transpose transformation, and the symbol * stands for an element-by-element row or column multiplication. That is, each column of the FFT of $\mathbf{\Phi_{cond}}$ is multiplied element-by-element by the FFT of $\mathbf{Z_B}$, and each row of the resulting matrix is multiplied element-by-element by the transposed FFT of $\mathbf{Z_A}$. The inverse FFT of this product gives directly the inductances matrix $\mathbf{L_{BA}}$.

Equation (62) is based on the convolution theorem, which states that the FT of the convolution of two functions is equal to the product of the FTs of both functions. In [82] this theorem was applied to the computation of phase inductances, using 1D matrices for representing the phase conductor distributions and the yoke flux generated by a single conductor. Equation (62) is an extension of this procedure to the case of an eccentric machine, where the yoke flux generated by a conductor must be represented using a full 3D matrix $\mathbf{\Phi_{cond}}$, to take into account the influence of the rotor centre position.

The expression (62) can be programmed very easily in commercial software packages. For example, in MATLAB language it is simply written as

$$\texttt{LBA} = \texttt{ifftn}(\ (\texttt{fft(ZA)}.' \ .*\ \texttt{fftn(PhyCond)}\ .*\ \texttt{fft(ZB)})\ ) \tag{63}$$

For a given IM, it is necessary to compute the inductance matrices $\mathbf{L_{ss}}$, $\mathbf{L_{rr}}$, $\mathbf{L_{sr}}$ and $\mathbf{L_{rs}}$, which are used in eqs (3) to (8). Denoting $\mathbf{Z_s}$ as the distribution of the conductors or a stator phase (assuming that all the stator phases are identical), and $\mathbf{Z_r}$ as the distribution of the conductors or a rotor phase (assuming also that all the rotor phases are identical), (62) must be particularized for the following cases:

- Phases A and B in the stator ($\mathbf{Z_A} = \mathbf{Z_B} = \mathbf{Z_s}$)

$$\mathbf{L_{ss}} = \mathrm{IFFT}\Big\{ \Big((\mathrm{FFT}\{\mathbf{Z_s}\})' \ * \ \mathrm{FFT}\{\mathbf{\Phi_{cond}}\} \ * \ \mathrm{FFT}\{\mathbf{Z_s}\} \Big) \Big\} \tag{64}$$

- Phases A and B in the rotor ($\mathbf{Z_A} = \mathbf{Z_B} = \mathbf{Z_r}$)

$$\mathbf{L_{rr}} = \mathrm{IFFT}\Big\{ \Big((\mathrm{FFT}\{\mathbf{Z_r}\})' \ * \ \mathrm{FFT}\{\mathbf{\Phi_{cond}}\} \ * \ \mathrm{FFT}\{\mathbf{Z_r}\} \Big) \Big\} \tag{65}$$

- Phase A in the stator ($\mathbf{Z_A} = \mathbf{Z_s}$) and phase B in the rotor ($\mathbf{Z_B} = \mathbf{Z_r}$)

$$\mathbf{L_{sr}} = \mathrm{IFFT}\Big\{ \Big((\mathrm{FFT}\{\mathbf{Z_s}\})' \ * \ \mathrm{FFT}\{\mathbf{\Phi_{cond}}\} \ * \ \mathrm{FFT}\{\mathbf{Z_r}\} \Big) \Big\} \tag{66}$$

- Phase A in the rotor ($\mathbf{Z_A} = \mathbf{Z_r}$) and phase B in the stator ($\mathbf{Z_B} = \mathbf{Z_s}$)

$$\mathbf{L_{rs}} = \text{IFFT}\Big\{ \Big((\text{FFT}\{\mathbf{Z_r}\})' \, * \, \text{FFT}\{\mathbf{\Phi_{cond}}\} \, * \, \text{FFT}\{\mathbf{Z_s}\}\Big) \Big\} \quad (67)$$

It is worth mentioning that, in equations (64), (65), (66) and (67), the term $\mathbf{\Phi_{cond}}$ is the same. Therefore, it must be computed just once. Moreover, this term is valid for all IM machines with the same degree of eccentricity, except from a scale factor $\frac{\mu_0 l r}{g_0}$ (44). Besides, $\mathbf{L_{rs}} = \mathbf{L_{sr}}'$, which makes unnecessary to compute (67).

The distribution of the phase conductors $\mathbf{Z_A}$ in (60) and $\mathbf{Z_B}$ in (61) have been assumed aligned with the d-axis, for simplicity of (62). If this condition is not met, by choosing other origin of angular coordinates, and the distribution of conductors is not symmetric with respect to this new origin, then FFT$\{\mathbf{Z_A}\}$ and FFT$\{\mathbf{Z_B}\}$ in (62) must be replaced by their conjugates, that is, conj(FFT$\{\mathbf{Z_A}\}$) and conj(FFT$\{\mathbf{Z_B}\}$).

8. Numerical and Experimental Validation

The method proposed in this paper has been validated, both numerically and experimentally, using a commercial IM whose characteristics are given in Appendix A. A mixed eccentricity is introduced in this IM, characterized by δ_{se}=0.3 and δ_{de}=0.3.

8.1. Numerical Validation

For the numerical validation of the proposed method, a finite element model (FEM) of the motor has been implemented using FEMM software [99]. For this simulation, a value of N=1008 rotor positions has been selected, obtained by multiplying the rotor and the stator number of slots. For each rotor position, one of the machine phases is fed with an unit current, and the flux linkages of all the phases are computed, giving their mutual inductances. The same procedure is repeated for all the IM phases, and for all rotor positions, giving a total number of simulations equal to $31 \times 1008 = 31248$ simulations, with a total time of 1300 hours, using the computer of Appendix C. Fig. 18 shows the simulations for a rotor position at the origin, for the first phase of the stator (Fig. 18, top) and of the first rotor loop, constituted by two adjacent bars and their end-ring connections (Fig. 18, bottom).

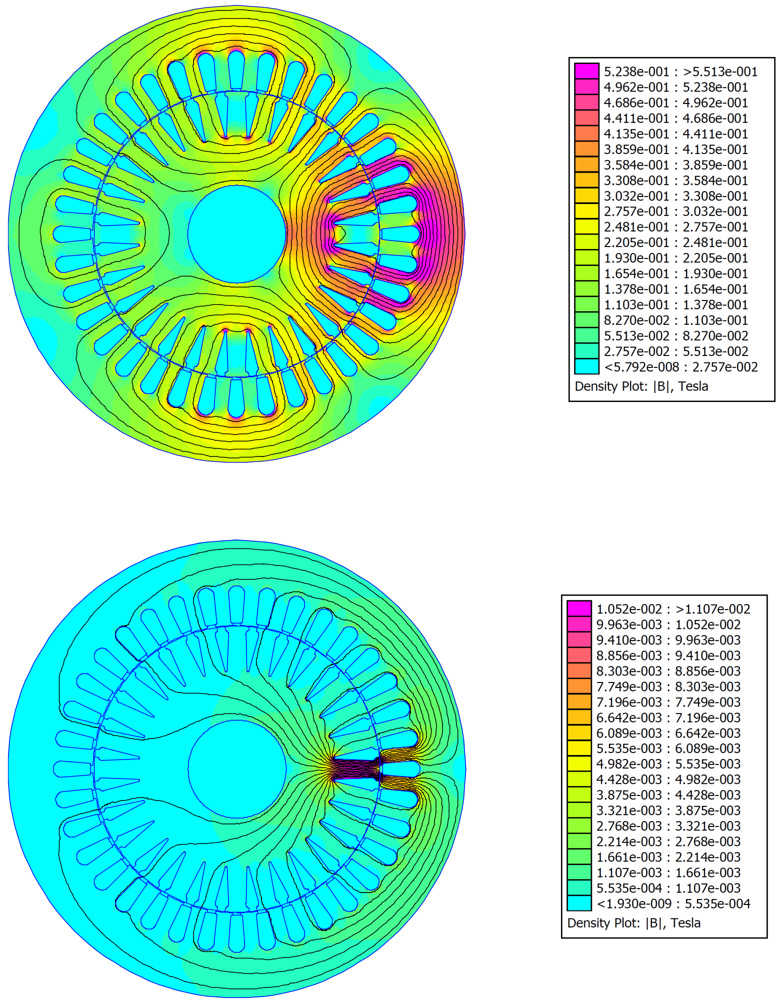

Figure 18: Simulation of the IM of Appendix A with an eccentricity degree of $\delta_{se} = 0.3$ and $\delta_{de} = 0.3$. Top: first stator phase fed with a unit current. Bottom: first rotor loop fed with a unit current.

The same machine has been simulated with the method proposed in this paper. The analytical solution, which gives the mutual inductances between all the phases for the N=1008 different angular rotor positions, has been obtained in just 10 minutes, using the same computer of Appendix C. Fig. 19 compares the inductances calculated for 1008 different rotor positions, using the FEM, and the proposed analytical method. In both cases, the machine of Appendix A is used, with a mixed eccentricity characterized by by δ_{se}=0.3 and δ_{de}=0.3. Fig. 19, top, compares the self inductance of the stator phase A for different positions of the rotor. Fig. 19, middle, compares the self inductance of the first rotor loop for different positions of the rotor. Finally, Fig. 19, bottom, compares the mutual inductance between stator phase A and the first rotor loop for different positions of the rotor. A good agreement is observed in the three comparisons of Fig. 19. The analytical model, unlike the FEM model, does not take into account the influence of slotting, but, except this difference, the changes of the inductances produced by the rotor position is very similar with both models.

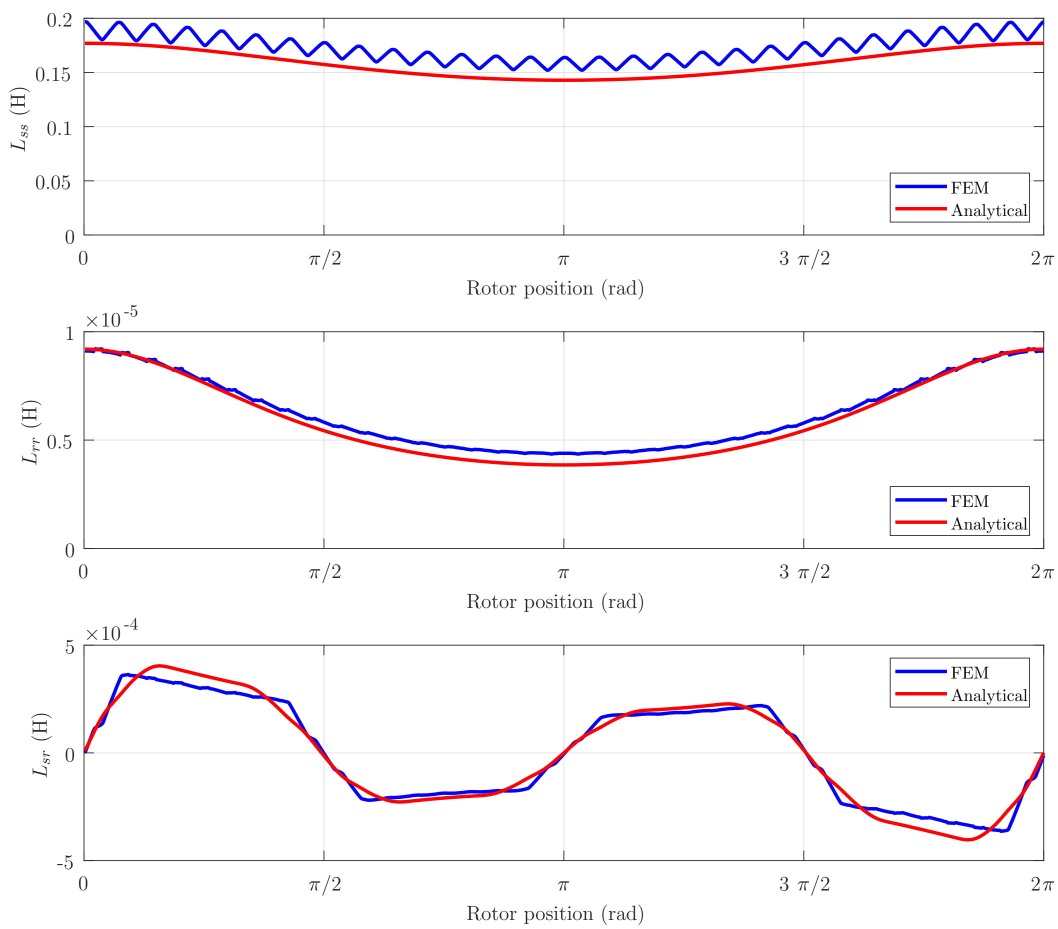

Figure 19: Comparison between the inductances obtained via FEM simulation (blue line) and with the proposed analytical method (red line), for the IM of Appendix A with an eccentricity degree of $\delta_{se} = 0.3$ and $\delta_{de} = 0.3$. Top: self-inductance of the first stator phase. Middle: self-inductance of the first rotor loop. Bottom: mutual inductance between the first stator phase and the first rotor loop.

To further assess the validity of the proposed method, the IM of Appendix A has been simulated with six different degrees of static and dynamic eccentricity (δ_{se}, δ_{de}), summarized in Table 2

Table 2: Degrees of static and dynamic eccentricity of the six simulated and experimental cases used in this work

Case N.	δ_{se}	δ_{de}	Remark
1	0.0	0.0	Healthy machine
2	0.6	0.0	Static eccentricity
3	0.4	0.2	Mixed eccentricity
4	0.3	0.3	Mixed eccentricity
5	0.2	0.4	Mixed eccentricity
6	0.0	0.6	Dynamic eccentricity

Fig. 20 shows the comparison of the mutual inductance between the first stator phase and the first rotor loop obtained for the machine in Appendix A via FEM simulation (top) and with the proposed analytical method (bottom), corresponding to the six cases summarized in Table 2. Fig 21 provides the same comparison for the self inductance of the first rotor loop, and Fig. 22 provides the same comparison for the self inductance of the first stator phase.

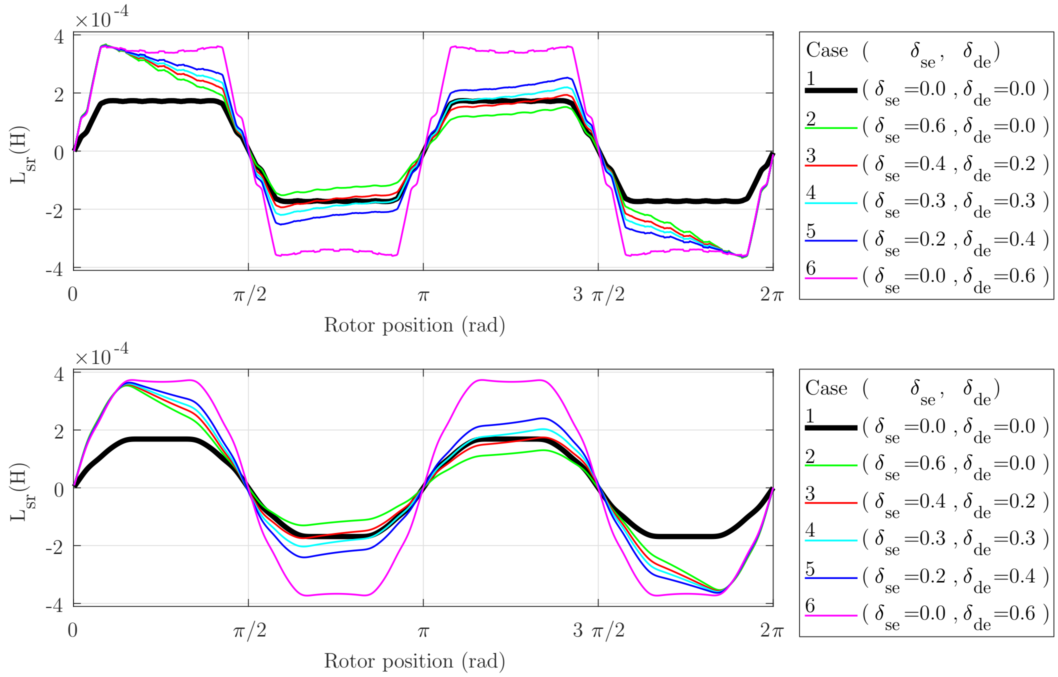

Figure 20: Comparison of the evolution of the mutual inductance against the rotor position between the first stator phase and the first rotor loop obtained for the machine in Appendix A via FEM simulation (top) and with the proposed analytical method (bottom). Six different degrees of static and dynamic eccentricity (δ_{se},δ_{de}) have been plotted: (0.0, 0.0),(0.6, 0.0), (0.4, 0.2), (0.3, 0.3), (0.2, 0.4) and (0.0, 0.6).

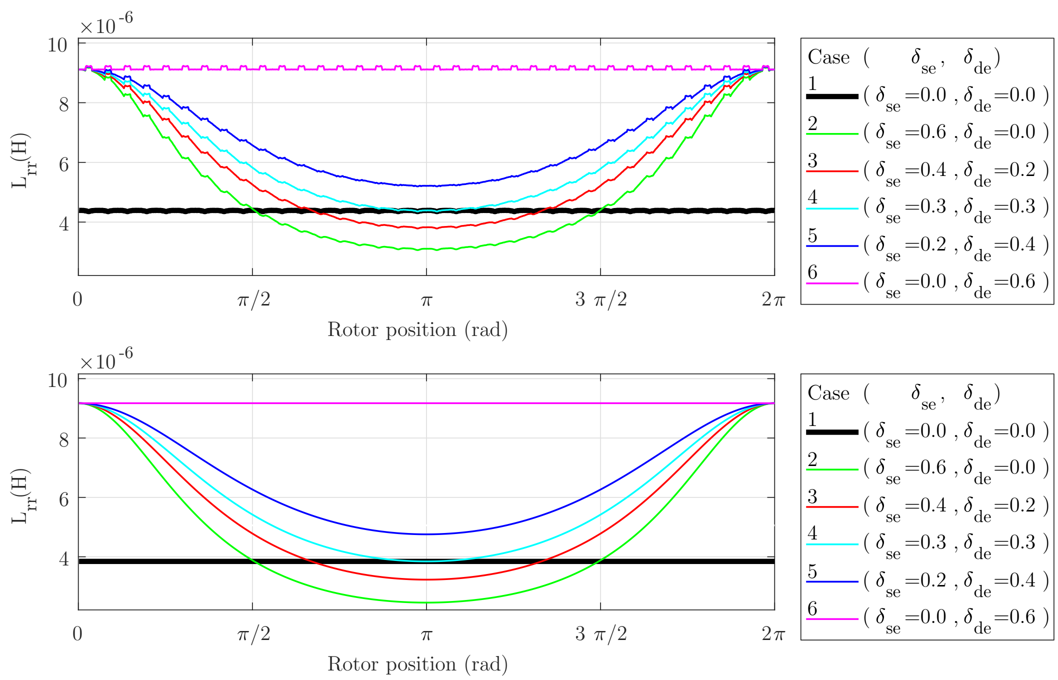

Figure 21: Comparison of the evolution of the self inductance of the first rotor loop against the rotor position obtained for the machine in Appendix A via FEM simulation (top) and with the proposed analytical method (bottom). Six different degrees of static and dynamic eccentricity (δ_{se},δ_{de}) have been plotted: (0.0, 0.0),(0.6, 0.0), (0.4, 0.2), (0.3, 0.3), (0.2, 0.4) and (0.0, 0.6).

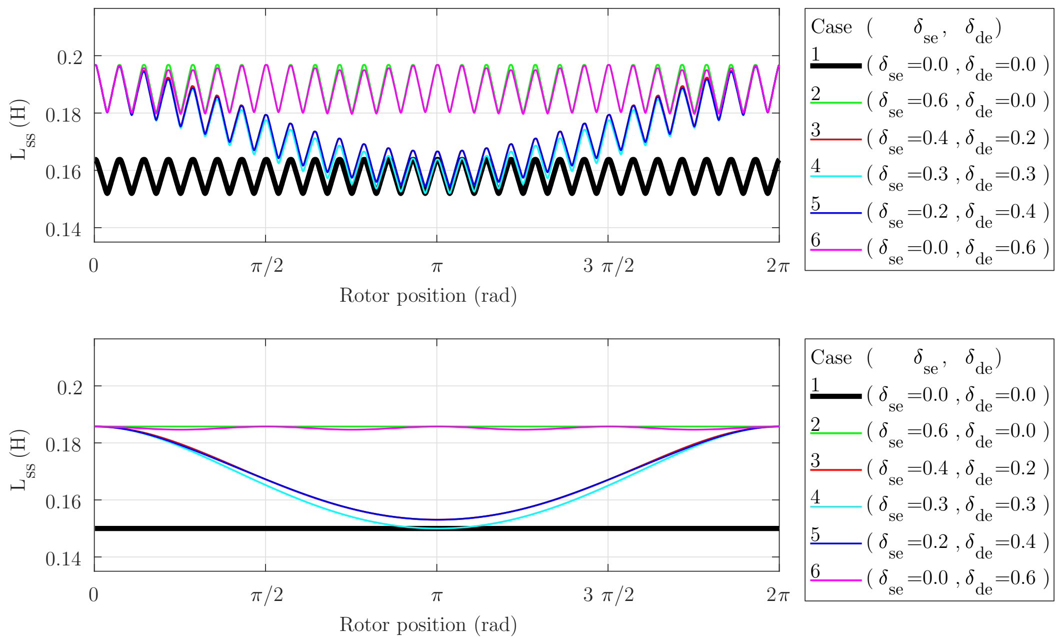

Figure 22: Comparison of the evolution of the self inductance of the first stator phase against the rotor position obtained for the machine in Appendix A via FEM simulation (top) and with the proposed analytical method (bottom). Six different degrees of static and dynamic eccentricity (δ_{se},δ_{de}) have been plotted: (0.0, 0.0),(0.6, 0.0), (0.4, 0.2), (0.3, 0.3), (0.2, 0.4) and (0.0, 0.6).

Figures 20, 21 and 22 show a good agreement between the inductances calculated using the proposed analytical method, and with the FEM model, apart from slotting effects that are not included in the analytical model.

8.2. Experimental Validation

For the experimental validation of the suitability of the proposed analytical model of eccentric IM for diagnostic purposes, the motor whose characteristics are given in Appendix A has been endowed with an artificially provoked mixed eccentricity fault. For this purpose, each original bearing of the motor (see Fig.23.a) has been substituted by a new bearing (Fig. 23.d) with smaller outer diameter and greater inner diameter. Also two precision eccentric machined steel rings (Fig. 23.b and Fig. 23.c) have been used for adjusting the new bearing to the bearing housing (Fig. 23.b) and to the shaft (Fig. 23.c). The cylindrical surfaces of both rings are eccentric, 0.4 mm in the case of the outer ring b, and 0.4 mm in the case of the inner ring c. Fig.

23.e shows the new assembly mounted on the shaft, obtaining in this way a rotor with a 30% of static eccentricity and a 30% of dynamic eccentricity.

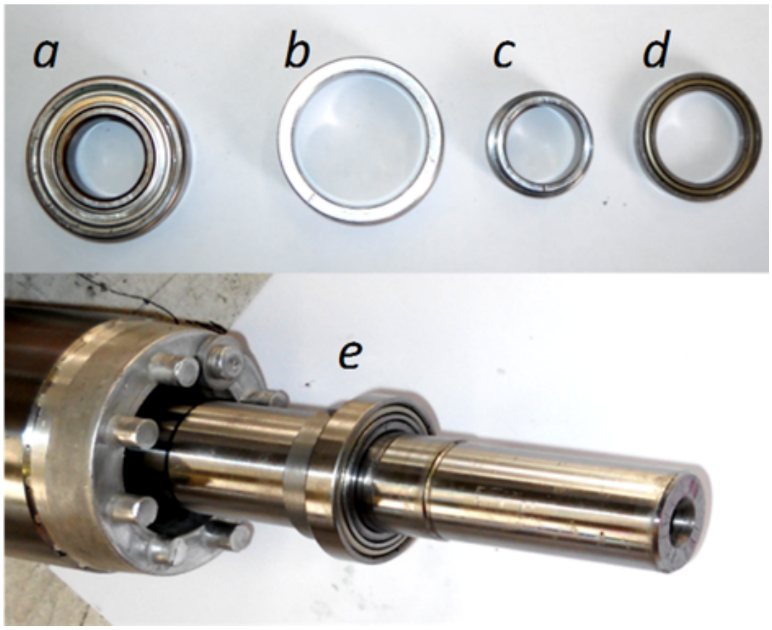

Figure 23: Rotor of the eccentric motor unit. Top, from left to right: a) original bearing, b) external and c) internal eccentric rings, and d) new bearing. Bottom: e) mounted unit on the shaft.

In the case of mixed eccentricity, it is well known in the technical literature [100] that this type of fault generates two different series of harmonics in the line current spectrum: a high frequency series of harmonics, which appear as sidebands around the principal slot harmonics, and a low frequency series of harmonics, which appear as sidebands around the fundamental component, at frequencies given by

$$f_{ME}(s) = f_1 \pm (k\ (1-s) f_1/p)\,, \quad k = 1, 2, 3\dots \tag{68}$$

where f_1 is the power supply frequency, s is the slip and p is the number of pole pairs of the machine.

Focusing on the most dominant component of the series (68), obtained with $k = 1$, a mixed eccentricity fault can be characterized by the presence in the stator current spectrum of components with frequencies given by:

$$f_{ME}(s) = f_1 \pm (1-s)f_1/p = f_1 \pm f_r \tag{69}$$

where f_r is the rotational frequency of the motor. In the case of the tested motor, with $p = 2$, (69) becomes

$$f_{ME}(s) = f_1 \pm (1-s)f_1/2 \tag{70}$$

To verify the validity of the method proposed in this paper to reproduce the fault harmonics at frequencies given by (70), the commercial motor Appendix A has been tested at a speed of 1488 rpm ($s = (1500-1488)/1500 = 0.008$), under two different conditions:

- In healthy state, before mounting the eccentricity rings.
- Under faulty conditions, after mounting the eccentricity rings.

In both cases, one of the phase currents has been acquired, using the current clamp whose data is given in Appendix B, during an acquisition time of 10 seconds, with a sampling frequency of 5 kHz. The spectra of these currents are shown in 24 for the case of the motor in healthy condition (24, top) and with the eccentricity rings mounted (24, bottom). As expected from (70), two fault related harmonics appear in faulty conditions at frequencies $f_{ME}(0.008) = 50 \pm (1-0.008)50/2 =$ [25.2 Hz, 74.8 Hz].

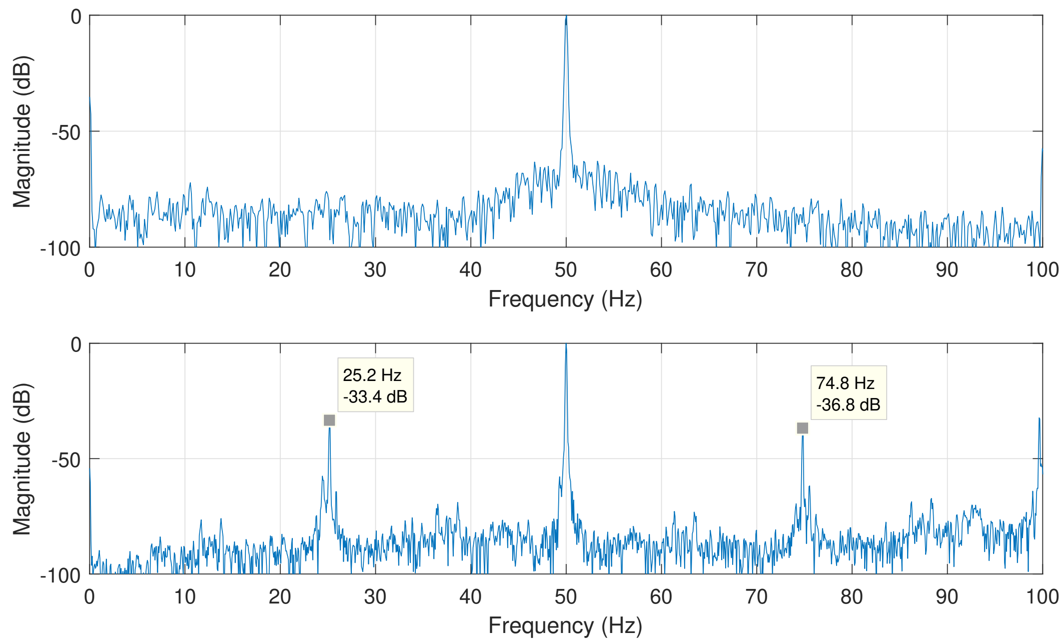

Figure 24: Spectra of the experimental current of the motor Appendix A for the case of the motor in healthy condition (24, top) and with the eccentricity ring mounted (24, bottom). As expected from (70), two fault related harmonics appear in faulty conditions at frequencies $f_{ME}(0.008) = 50 \pm (1 - 0.008)50/2 = [25.2 \text{ Hz}, 74.8 \text{ Hz}]$.

The motor of Appendix A has been simulated under the same conditions as the experimental test, 1488 rpm, both in healthy and faulty conditions, using the Simulink model given in [82]. In this model, the phases inductance matrix at each simulation time step is updated according to the rotor angular position, using the inductances matrix and its angular derivative that have been computed previously with (64),(65) and (66). The spectra of the stator phase current obtained from the simulation are given in Fig. 25,top, for the healthy condition, and in Fig. 25,bottom, for the eccentric fault condition. As Fig. 25 shows, the inductances matrix obtained with the method proposed in this paper is able to correctly reproduce the fault harmonics generated by a mixed eccentricity fault (25, bottom), predicting accurately the frequencies of the fault components, and also giving a good approximation for their amplitudes.

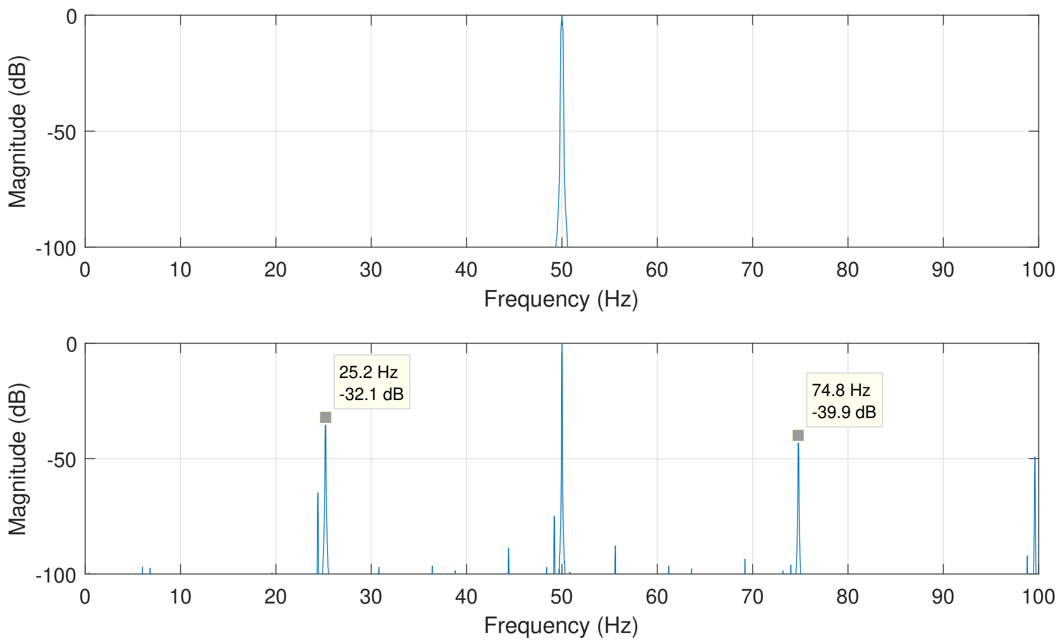

Figure 25: Spectrum of the stator phase current obtained from the simulation of the motor referenced in Appendix A in healthy condition (top), and with a mixed eccentricity of (δ_{se},δ_{de})=(0.3, 0.3) (bottom). These spectra show that the inductances matrix obtained with the method proposed in this paper is able to correctly reproduce the fault harmonics generated by a mixed eccentricity fault.

9. Conclusions

In this paper, a novel approach for computing the phases inductances of an eccentric IM has been presented. These inductances can be used in analytical models in order to reproduce the fault harmonics that are characteristic of an eccentricity fault, which can be used for the development of advanced fault diagnostic algorithms, or for training expert systems. The proposed method relies on two main novelties: first, an analytical expression for the yoke flux produced by a single conductor in an eccentric machine, as a function of the conductor and rotor position, and of the degree of static and dynamic eccentric, has been obtained; and second, using this expression, a convolution-based procedure has been proposed for obtaining the inductances matrix which gives the self and mutual inductances for every phases and rotor positions, by a simple product in the spatial frequency domain, implemented with the FFT. The proposed convolution-based method enables to calculate the inductances matrix in few minutes, instead of hundreds of hours that will take this calculation using a FEM model. It is noticeable that, for a given degree of dynamic and static eccentricity, the inductances matrix is valid, except for a scale factor, for any IM. The proposed method has been validated by comparing it with a FEM model, and with the results obtained from experimental tests with a commercial IM with a forced eccentricity fault. The extension of the proposed model to include axial and curved eccentricity faults is currently under work.

Appendix A. Commercial IM

Three-phase induction machine. Rated characteristics: $P = 1.1$ kW, $f = 50$ Hz, $U = 230/400$ V, $I = 2.7/4.6$ A, $n = 1410$ r/min , $\cos\varphi = 0.8$.

Machine dimensions: Effective length of the magnetic core = 70.2 mm, radius at the middle of the air gap = 41.1 mm, air gap length = 1.2 mm.

Stator: Three-phase winding, 36 slots, 78 wires/slot, winding pitch = 7/9, slot opening width = 2.1 mm, phase resistance 7.68 Ω, end winding leakage = 2.3 mH.

Rotor: Squirrel-cage winding, 28 bars, slot opening width = 1.4 mm, skew = one slot pitch, bar resistance = 0.00202 mΩ, end winding leakage = 2.45×10^{-5} mH.

Appendix B. Current Clamp

Chauvin Arnoux MN60, Nominal measuring scope: 100 mA–20A, ratio input/output: 1 A/100 mV, intrinsic error: $\leq 2\% + 50$ mV, frequency use: 400 Hz–10 kHz.

Appendix C. Computer Features

CPU: Intel Core i7-2600K CPU @ 3.40 GHZ RAM memory: 16 GB, Matlab Version: 9.4.0.813654 (R2018a).

Acknowledgements

This work was supported by the Spanish "Ministerio de Ciencia, Innovación y Universidades (MCIU)", the "Agencia Estatal de Investigación (AEI)" and the "Fondo Europeo de Desarrollo Regional (FEDER)" in the framework of the "Proyectos I+D+i - Retos Investigación 2018", project reference RTI2018-102175-B-I00 (MCIU/AEI/FEDER, UE).

References

References

[1] Y. Liu, A. M. Bazzi, A review and comparison of fault detection and diagnosis methods for squirrel-cage induction motors: State of the art, ISA Trans. 70 (2017) 400–409.

[2] L. A. Trujillo-Guajardo, J. Rodriguez-Maldonado, M. A. Moonem, M. A. Platas-Garza, A Multiresolution Taylor-Kalman Approach for Broken Rotor Bar Detection in Cage Induction Motors, IEEE Trans. Instrum. Meas. 67 (2018) 1317–1328.

[3] P. B. Dao, W. J. Staszewski, T. Barszcz, T. Uhl, Condition monitoring and fault detection in wind turbines based on cointegration analysis of SCADA data, Renew. Energy 116 (2018) 107–122.

[4] H. Garg, R. Dahiya, Current signature analysis and its application in the condition monitoring of wind turbine for rotor faults, Energy Syst. 8 (2017) 495–510.

[5] A. Balasubramanian, R. Muthu, Model Based Fault Detection and Diagnosis of Doubly Fed Induction Generators - A Review, Energy Procedia 117 (2017) 935–942.

[6] A. Bellini, F. Filippetti, C. Tassoni, G.-A. Capolino, Advances in Diagnostic Techniques for Induction Machines, IEEE Trans. Ind. Electron. 55 (2008) 4109–4126.

[7] I. Culbert, J. Letal, Signature Analysis for Online Motor Diagnostics: Early Detection of Rotating Machine Problems Prior to Failure, IEEE Ind. Appl. Mag. 23 (2017) 76–81.

[8] M. Manohar, E. Koley, S. Ghosh, Enhancing resilience of PV-fed microgrid by improved relaying and differentiating between inverter faults and distribution line faults, Int. J. Electr. Power Energy Syst. 108 (2019) 271–279.

[9] X. Xia, J. Zhou, C. Li, W. Zhu, A novel method for fault diagnosis of hydro generator based on NOFRFs, Int. J. Electr. Power Energy Syst. 71 (2015) 60–67.

[10] B. Zhao, M. Yang, H. Diao, B. An, Y. Zhao, Y. Zhang, A novel approach to transformer fault diagnosis using IDM and naive credal classifier, Int. J. Electr. Power Energy Syst. 105 (2019) 846–855.

[11] M. H. Samimi, A. A. Shayegani Akmal, H. Mohseni, S. Tenbohlen, Detection of transformer mechanical deformations by comparing different FRA connections, Int. J. Electr. Power Energy Syst. 86 (2017) 53–60.

[12] G. Rigatos, P. Siano, Power transformers' condition monitoring using neural modeling and the local statistical approach to fault diagnosis, Int. J. Electr. Power Energy Syst. 80 (2016) 150–159.

[13] S. S. Ghoneim, I. B. Taha, A new approach of DGA interpretation technique for transformer fault diagnosis, Int. J. Electr. Power Energy Syst. 81 (2016) 265–274.

[14] Y. Zhang, Y. Zhang, F. Wen, C. Y. Chung, C.-L. Tseng, X. Zhang, F. Zeng, Y. Yuan, A fuzzy Petri net based approach for fault diagnosis in power systems considering temporal constraints, Int. J. Electr. Power Energy Syst. 78 (2016) 215–224.

[15] M. Farshad, Detection and classification of internal faults in bipolar HVDC transmission lines based on K-means data description method, Int. J. Electr. Power Energy Syst. 104 (2019) 615–625.

[16] P. R. N. da Silva, H. A. Gabbar, P. Vieira Junior, C. T. da Costa Junior, A new methodology for multiple incipient fault diagnosis in transmission lines using QTA and Naïve Bayes classifier, Int. J. Electr. Power Energy Syst. 103 (2018) 326–346.

[17] M. M. Morato, D. J. Regner, P. R. Mendes, J. E. Normey-Rico, C. Bordons, Fault Analysis, Detection and Estimation for a Microgrid via $H2/H^{\infty}$LPV Observers, Int. J. Electr. Power Energy Syst. 105 (2019) 823–845.

[18] T. Gush, S. B. A. Bukhari, R. Haider, S. Admasie, Y.-S. Oh, G.-J. Cho, C.-H. Kim, Fault detection and location in a microgrid using mathematical morphology and recursive least square methods, Int. J. Electr. Power Energy Syst. 102 (2018) 324–331.

[19] F. Garramiola, J. Poza, P. Madina, J. del Olmo, G. Almandoz, F. Garramiola, J. Poza, P. Madina, J. Del Olmo, G. Almandoz, A Review in Fault Diagnosis and Health Assessment for Railway Traction Drives, Appl. Sci. 8 (2018) 2475.

[20] M. Harir, A. Bendiabdellah, Stator Current Spectral content of an Induction Motor taking into account Saturation Effect, PRZEGLĄD ELEKTROTECHNICZNY (2018) 108–112.

[21] K. Yahia, M. Sahraoui, A. J. M. Cardoso, A. Ghoggal, The Use of a Modified Prony's Method to Detect the Airgap-Eccentricity Occurrence in Induction Motors, IEEE Trans. Ind. Appl. 52 (2016) 3869–3877.

[22] E. H. El Bouchikhi, V. Choqueuse, M. Benbouzid, Induction machine faults detection using stator current parametric spectral estimation, Mech. Syst. Signal Process. 52-53 (2015) 447–464.

[23] C. Bruzzese, Diagnosis of Eccentric Rotor in Synchronous Machines by Analysis of Split-Phase CurrentsâĂŤPart I: Theoretical Analysis, IEEE Trans. Ind. Electron. 61 (2014) 4193–4205.

[24] N. Bessous, S. E. Zouzou, S. Sbaa, W. Bentrah, A comparative study between the MCSA, DWT and the vibration analysis methods to diagnose the dynamic eccentricity fault in induction motors, in: 2017 6th Int. Conf. Syst. Control, IEEE, 2017, pp. 414–421.

[25] C. Morales-Perez, J. Rangel-Magdaleno, H. Peregrina-Barreto, J. P. Amezquita-Sanchez, M. Valtierra-Rodriguez, Incipient Broken Rotor Bar Detection in Induction Motors Using Vibration Signals and the Orthogonal Matching Pursuit Algorithm, IEEE Trans. Instrum. Meas. 67 (2018) 2058–2068.

[26] F. Çira, Detection of eccentricity fault based on vibration in the PMSM, Results Phys. 10 (2018) 760–765.

[27] Y. Li, F. Chai, Z. Song, Z. Li, Y. Li, F. Chai, Z. Song, Z. Li, Analysis of Vibrations in Interior Permanent Magnet Synchronous Motors Considering Air-Gap Deformation, Energies 10 (2017) 1259.

[28] J. Faiz, M. Ojaghi, Instantaneous-Power Harmonics as Indexes for Mixed Eccentricity Fault in Mains-Fed and Open/Closed-Loop Drive-Connected Squirrel-Cage Induction Motors, IEEE Trans. Ind. Electron. 56 (2009) 4718–4726.

[29] J. Faiz, S. M. M. Moosavi, Detection of mixed eccentricity fault in doubly-fed induction generator based on reactive power spectrum, IET Electr. Power Appl. 11 (2017) 1076–1084.

[30] M. E. K. Oumaamar, Y. Maouche, M. Boucherma, A. Khezzar, Static air-gap eccentricity fault diagnosis using rotor slot harmonics in line neutral voltage of three-phase squirrel cage induction motor, Mech. Syst. Signal Process. 84 (2017) 584–597.

[31] M. E. K. Oumaamar, Y. Maouche, M. Boucherma, A. Khezzar, Static air-gap eccentricity fault diagnosis using rotor slot harmonics in line neutral voltage of three-phase squirrel cage induction motor, Mech. Syst. Signal Process. 84 (2017) 584–597.

[32] K. Kang, J. Song, C. Kang, S. Sung, G. Jang, Real-Time Detection of the Dynamic Eccentricity in Permanent-Magnet Synchronous Motors by Monitoring Speed and Back EMF Induced in an Additional Winding, IEEE Trans. Ind. Electron. 64 (2017) 7191–7200.

[33] E. Ajily, M. Ardebili, K. Abbaszadeh, Magnet Defect and Rotor Eccentricity Modeling in Axial-Flux Permanent-Magnet Machines via 3-D Field Reconstruction Method, IEEE Trans. Energy Convers. 31 (2016) 486–495.

[34] Z. Liu, J. Huang, S. He, Diagnosis of air-gap eccentricity and partial demagnetisation of an interior permanent magnet synchronous motor based on inverse transient complex inductance vector theory, IET Electr. Power Appl. 12 (2018) 1166–1175.

[35] A. Glowacz, Z. Glowacz, Diagnosis of the three-phase induction motor using thermal imaging, Infrared Phys. Technol. 81 (2017) 7–16.

[36] E. Resendiz-Ochoa, R. A. Osornio-Rios, J. P. Benitez-Rangel, R. De J. Romero-Troncoso, L. A. Morales-Hernandez, Induction Motor Failure Analysis: An Automatic Methodology Based on Infrared Imaging, IEEE Access 6 (2018) 76993–77003.

[37] G. Mirzaeva, K. I. Saad, Advanced Diagnosis of Stator Turn-to-Turn Faults and Static Eccentricity in Induction Motors Based on Internal Flux Measurement, IEEE Trans. Ind. Appl. 54 (2018) 3961–3970.

[38] Y. Soleimani, S. M. A. Cruz, F. Haghjoo, Broken Rotor Bar Detection in Induction Motors Based on Air-Gap Rotational Magnetic Field Measurement, IEEE Trans. Instrum. Meas. (2018) 1–10.

[39] P. S. B, S. Hemamalini, Rational-Dilation Wavelet Transform based Torque Estimation from Acoustic signals for Fault Diagnosis in a Three Phase Induction Motor, IEEE Trans. Ind. Informatics (2018) 1–1.

[40] D.-J. Kim, H.-J. Kim, J.-P. Hong, C.-J. Park, Estimation of Acoustic Noise and Vibration in an Induction Machine Considering Rotor Eccentricity, IEEE Trans. Magn. 50 (2014) 857–860.

[41] A. Naha, A. K. Samanta, A. Routray, A. K. Deb, Low Complexity Motor Current Signature Analysis Using Sub-Nyquist Strategy With Reduced Data Length, IEEE Trans. Instrum. Meas. 66 (2017) 3249–3259.

[42] J. De Bisschop, P. Sergeant, A. Hemeida, H. Vansompel, L. Dupre, Analytical Model for Combined Study of Magnet Demagnetization and Eccentricity Defects in Axial Flux Permanent Magnet Synchronous Machines, IEEE Trans. Magn. 53 (2017) 1–12.

[43] M. Kaikaa, Effect of unbalanced supply on dynamic eccentricity fault diagnosis in induction motor, Int. J. Appl. Electromagn. Mech. 46 (2014) 793–808.

[44] M. Y. Kaikaa, M. Hadjami, A. Khezzar, Effects of the simultaneous presence of static eccentricity and broken rotor bars on the stator current of induction machine, IEEE Trans. Ind. Electron. 61 (2014) 2452–2463.

[45] G. Singh, V. Naikan, Detection of half broken rotor bar fault in VFD driven induction motor drive using motor square current MUSIC analysis, Mech. Syst. Signal Process. 110 (2018) 333–348.

[46] D. Morinigo-Sotelo, L. Garcia-Escudero, O. Duque-Perez, M. Perez-Alonso, Practical Aspects of Mixed-Eccentricity Detection in PWM

Voltage-Source-Inverter-Fed Induction Motors, IEEE Trans. Ind. Electron. 57 (2010) 252–262.

[47] P. Gangsar, R. Tiwari, A support vector machine based fault diagnostics of Induction motors for practical situation of multi-sensor limited data case, Meas. J. Int. Meas. Confed. 135 (2019) 694–711.

[48] A. Singh, B. Grant, R. DeFour, C. Sharma, S. Bahadoorsingh, A review of induction motor fault modeling, Electr. Power Syst. Res. 133 (2016) 191–197.

[49] M. Ojaghi, R. Aghmasheh, M. Sabouri, Model-based exact technique to identify type and degree of eccentricity faults in induction motors, IET Electr. Power Appl. 10 (2016) 706–713.

[50] A. A. Salah, D. G. Dorrell, Y. Guo, A Review of the Monitoring and Damping Unbalanced Magnetic Pull in Induction Machines Due to Rotor Eccentricity, IEEE Trans. Ind. Appl. (2019) 1–1.

[51] P. Naderi, F. Fallahi, Eccentricity fault diagnosis in three-phase-wound-rotor induction machine using numerical discrete modeling method, Int. J. Numer. Model. Electron. Networks, Devices Fields 29 (2016) 982–997.

[52] J. Faiz, S. Moosavi, Eccentricity fault detection - From induction machines to DFIG - A review, Renew. Sustain. Energy Rev. 55 (2016) 169–179.

[53] B. Silwal, P. Rasilo, L. Perkkio, A. Hannukainen, T. Eirola, A. Arkkio, Numerical Analysis of the Power Balance of an Electrical Machine With Rotor Eccentricity, IEEE Trans. Magn. 52 (2016) 1–4.

[54] B. Rajalakshmi Samaga, K. Vittal, Comprehensive study of mixed eccentricity fault diagnosis in induction motors using signature analysis, Int. J. Electr. Power Energy Syst. 35 (2012) 180–185.

[55] J. Faiz, M. Ojaghi, Different indexes for eccentricity faults diagnosis in three-phase squirrel-cage induction motors: A review, Mechatronics 19 (2009) 2–13.

[56] Y. Yao, Y. Li, Q. Yin, A novel method based on self-sensing motor drive system for misalignment detection, Mech. Syst. Signal Process. 116 (2019) 217–229.

[57] J. J. Perez-Loya, C. J. D. Abrahamsson, U. Lundin, Electromagnetic Losses in Synchronous Machines During Active Compensation of Unbalanced Magnetic Pull, IEEE Trans. Ind. Electron. 66 (2019) 124–131.

[58] Y. Zhou, X. Bao, C. Di, L. Wang, Analysis of Dynamic Unbalanced Magnetic Pull in Induction Motor With Dynamic Eccentricity During Starting Period, IEEE Trans. Magn. 52 (2016) 1–4.

[59] Chong Di, Xiaohua Bao, Hanfeng Wang, Qiang Lv, Yigang He, Modeling and Analysis of Unbalanced Magnetic Pull in Cage Induction Motors With Curved Dynamic Eccentricity, IEEE Trans. Magn. 51 (2015) 1–7.

[60] D. G. Dorrell, Sources and Characteristics of Unbalanced Magnetic Pull in Three-Phase Cage Induction Motors With Axial-Varying Rotor Eccentricity, IEEE Trans. Ind. Appl. 47 (2011) 12–24.

[61] A. Burakov, A. Arkkio, Comparison of the Unbalanced Magnetic Pull Mitigation by the Parallel Paths in the Stator and Rotor Windings, IEEE Trans. Magn. 43 (2007) 4083–4088.

[62] X. Xu, Q. Han, F. Chu, A general electromagnetic excitation model for electrical machines considering the magnetic saturation and rub impact, J. Sound Vib. 416 (2018) 154–171.

[63] J. Faiz, B. M. Ebrahimi, M. B. B. Sharifian, Finite Element Transient Analysis of an On-Load Three-Phase Squirrel-Cage Induction Motor with Static Eccentricity, Electromagnetics 27 (2007) 207–227.

[64] M. DeBortoli, S. Salon, D. Burow, C. Slavik, Effects of rotor eccentricity and parallel windings on induction machine behavior: a study using finite element analysis, IEEE Trans. Magn. 29 (1993) 1676–1682.

[65] J. Faiz, B. Ebrahimi, B. Akin, H. Toliyat, Comprehensive Eccentricity Fault Diagnosis in Induction Motors Using Finite Element Method, IEEE Trans. Magn. 45 (2009) 1764–1767.

[66] J. Martinez, A. Belahcen, J. Detoni, A. Arkkio, A 2D FEM analysis of electromechanical signatures in induction motors under dynamic eccentricity, Int. J. Numer. Model. Electron. Networks, Devices Fields 27 (2014) 555–571.

[67] M. Thiele, G. Heins, Computationally Efficient Method for Identifying Manufacturing Induced Rotor and Stator Misalignment in Permanent Magnet Brushless Machines, IEEE Trans. Ind. Appl. 52 (2016) 3033–3040.

[68] H. Mahmoud, N. Bianchi, Eccentricity in Synchronous Reluctance Motors - Part I: Analytical and Finite-Element Models, IEEE Trans. Energy Convers. 30 (2015) 745–753.

[69] T. Ilamparithi, S. Nandi, Comparison of results for eccentric cage induction motor using Finite Element method and Modified Winding Function Approach, in: 2010 Jt. Int. Conf. Power Electron. Drives Energy Syst. 2010 Power India, IEEE, 2010, pp. 1–7.

[70] J. Faiz, M. Ghasemi-Bijan, B. Mahdi Ebrahimi, Modeling and Diagnosing Eccentricity Fault Using Three-dimensional Magnetic Equivalent Circuit Model of Three-phase Squirrel-cage Induction Motor, Electr. Power Components Syst. 43 (2015) 1246–1256.

[71] S. Taghipour Boroujeni, P. Emami, P. Jalali, Analytical Modeling of Eccentric PM-inset machines with a Slotless Armature, IEEE Trans. Energy Convers. (2019) 1–1.

[72] P. Jalali, S. T. Boroujeni, N. Bianchi, Analytical Modeling of Slotless Eccentric Surface-Mounted PM Machines Using a Conformal Transformation, IEEE Trans. Energy Convers. 32 (2017) 658–666.

[73] B. Rezaeealam, F. Rezaee-Alam, An improved conformal mapping method for magnetic field analysis in surface mounted permanent magnet motors, COMPEL - Int. J. Comput. Math. Electr. Electron. Eng. 36 (2017) 2016–0284.

[74] A. Tessarolo, C. Bruzzese, Study of eccentric round-rotor synchronous machines through conformal mapping. Part I: Inductances and air-gap field, in: 2016 Elev. Int. Conf. Ecol. Veh. Renew. Energies, IEEE, 2016, pp. 1–7.

[75] K. Abbaszadeh, F. Rezaee Alam, On-Load Field Component Separation in Surface-Mounted Permanent-Magnet Motors Using an Improved Conformal Mapping Method, IEEE Trans. Magn. 52 (2016) 1–12.

[76] F. R. Alam, K. Abbaszadeh, Magnetic Field Analysis in Eccentric Surface-Mounted Permanent-Magnet Motors Using an Improved Conformal Mapping Method, IEEE Trans. Energy Convers. 31 (2016) 333–344.

[77] M. Ojaghi, M. Sabouri, J. Faiz, Performance Analysis of Squirrel-Cage Induction Motors Under Broken Rotor Bar and Stator Inter-Turn Fault Conditions Using Analytical Modeling, IEEE Trans. Magn. 54 (2018) 1–5.

[78] X. Bao, Z. Cheng, C. Di, Current analysis of large submersible motor under curved eccentricity by multi-loop method, Int. J. Appl. Electromagn. Mech. 53 (2017) 63–76.

[79] A. Ghoggal, S. Zouzou, H. Razik, M. Sahraoui, A. Khezzar, An improved model of induction motors for diagnosis purposes - Slot skewing effect and air-gap eccentricity faults, Energy Convers. Manag. 50 (2009) 1336–1347.

[80] J. Faiz, M. Ojaghi, Unified winding function approach for dynamic simulation of different kinds of eccentricity faults in cage induction machines, IET Electr. Power Appl. 3 (2009) 461.

[81] H. A. Toliyat, T. A. Lipo, J. C. White, Analysis of a concentrated winding induction machine for adjustable speed drive applications. I. Motor analysis, IEEE Trans. Energy Convers. 6 (1991) 679–683.

[82] A. Sapena-Bano, J. Martinez-Roman, R. Puche-Panadero, M. Pineda-Sanchez, J. Perez-Cruz, M. Riera-Guasp, Induction machine model with space harmonics for fault diagnosis based on the convolution theorem, Int. J. Electr. Power Energy Syst. 100 (2018) 463–481.

[83] Y. Horen, P. Strajnikov, A. Kuperman, Simple mechanical parameters identification of induction machine using voltage sensor only, Energy Conversion and Management 92 (2015) 60 – 66.

[84] A. Chatterjee, D. Chatterjee, An improved excitation control technique of three-phase induction machine operating as dual winding generator for micro-wind domestic application, Energy Conversion and Management 98 (2015) 98 – 106.

[85] M. Pineda-Sanchez, R. Puche-Panadero, J. Martinez-Roman, A. Sapena-Bano, M. Riera-Guasp, J. Perez-Cruz, Partial Inductance Model of Induction Machines for Fault Diagnosis, Sensors 18 (2018) 2340.

[86] M. Ikeda, T. Hiyama, Simulation Studies of the Transients of Squirrel-Ccage Induction Motors, IEEE Trans. Energy Convers. 22 (2007) 233–239.

[87] L. Alberti, N. Bianchi, S. Bolognani, A Very Rapid Prediction of IM Performance Combining Analytical and Finite-Element Analysis, IEEE Trans. Ind. Appl. 44 (2008) 1505–1512.

[88] J. Staszak, Determination of slot leakage inductance for three-phase induction motor winding using an analytical method, Archives of Electrical Engineering 62 (2013) 569 – 591.

[89] J. Faiz, I. Ardekanei, H. Toliyat, An evaluation of inductances of a squirrel-cage induction motor under mixed eccentric conditions, IEEE Trans. Energy Convers. 18 (2003) 252–258.

[90] H. Toliyat, M. Arefeen, A. Parlos, A method for dynamic simulation of air-gap eccentricity in induction machines, IEEE Trans. Ind. Appl. 32 (1996) 910–918.

[91] G. Joksimovic, M. Durovic, J. Penman, N. Arthur, Dynamic simulation of dynamic eccentricity in induction machines-winding function approach, IEEE Trans. Energy Convers. 15 (2000) 143–148.

[92] S. Nandi, S. Ahmed, H. Toliyat, Detection of rotor slot and other eccentricity related harmonics in a three phase induction motor with different rotor cages, IEEE Trans. Energy Convers. 16 (2001) 253–260.

[93] S. Nandi, R. Bharadwaj, H. Toliyat, Performance analysis of a three-phase induction motor under mixed eccentricity condition, IEEE Trans. Energy Convers. 17 (2002) 392–399.

[94] J. Faiz, I. Tabatabaei, Extension of winding function theory for nonuniform air gap in electric machinery, IEEE Trans. Magn. 38 (2002) 3654–3657.

[95] G. Bossio, C. De Angelo, J. Solsona, G. Garcia, M. I. Valla, A 2-D model of the induction machine: an extension of the modified winding function approach, Energy Conversion, IEEE Trans. 19 (2004) 144–150.

[96] B. Hague, The principles of electromagnetism applied to electrical machines, Dover, 1962.

[97] B. Heller, V. Hamata, Harmonic field effects in induction machines, Elsevier Science & Technology, 1977.

[98] X. Li, Q. Wu, S. Nandi, Performance Analysis of a Three-Phase Induction Machine With Inclined Static Eccentricity, IEEE Trans. Ind. Appl. 43 (2007) 531–541.

[99] D. Meeker, Finite Element Method Magnetics. User's Manual. Version 4.0, 2004.

[100] S. Nandi, R. M. Bharadwaj, H. A. Toliyat, Performance Analysis of a Three-Phase Induction Motor Under Mixed Eccentricity Condition, IEEE Trans. Energy Convers. 17 (2002) 392–399.